buildings

MDPI

Article

Hygrothermal Simulation of Interior Insulated Brick Wall—Perspectives on Uncertainty and Sensitivity

Jon Ivar Knarud [1,*], Tore Kvande [1] and Stig Geving [2]

[1] Department of Civil and Environmental Engineering, Norwegian University of Science and Technology, NO-7491 Trondheim, Norway; tore.kvande@ntnu.no
[2] Department of Architecture, Materials and Structures, SINTEF Community, NO-7465 Trondheim, Norway; stig.geving@sintef.no
* Correspondence: jon.knarud@ntnu.no; Tel.: +47-96019248

Abstract: Energy retrofit of existing masonry buildings has become attractive to meet demands for reduction in energy consumption. Retrofit may, however, introduce moisture risk that needs to be assessed. Hygrothermal simulation analysis is often conducted in this respect. Nevertheless, hygrothermal simulation of interior insulated bare brick masonry exposed to driving rain can be challenging due to the many aspects involved that determine heat- and moisture-transport behavior, and which should be addressed by an applied model. The present study highlights uncertainty encountered when establishing a hygrothermal simulation model. Furthermore, different modeling choices or simplifications are studied to determine impact on results. As a check of realism, results of 2D simulations are compared to results of a previous laboratory experiment of masonry wall segments subjected to severe rain wetting and subsequent drying. Rain absorption is modeled conservatively, attempting simulation results to envelope experiment results. Conservative results were not achieved for a relative humidity sensor placed on the masonry interior without inclusion of a "leaky" mortar joint. Simultaneously, the conservative approach underestimated drying experienced by the relative humidity sensor in two of three experiment wall segments. Regarding beam-end moisture content, the modeling approach conservatively enveloped experiment results in 3D but not in 2D.

Keywords: modeling approach; masonry wall; wooden beam ends; moisture absorption; capillary conductivity; brick–mortar interface; smart vapor barrier

Citation: Knarud, J.I.; Kvande, T.; Geving, S. Hygrothermal Simulation of Interior Insulated Brick Wall—Perspectives on Uncertainty and Sensitivity. *Buildings* **2023**, *13*, 1701. https://doi.org/10.3390/buildings13071701

Academic Editor: Chenggao Li

Received: 6 June 2023
Revised: 19 June 2023
Accepted: 29 June 2023
Published: 3 July 2023

1. Introduction

1.1. Context

In cold temperate climates, interior insulation is an important retrofit measure for older existing masonry buildings with exterior facades worth preserving. Compared to modern buildings following today's building regulations, masonry buildings from the period 1850–1950 have very high U-values. Interior insulation retrofit can by lowering U-values lower a high heating demand [1]. In combination with improving building envelope air tightness, utilizing heat recovery from ventilation, and, potentially, other measures, substantial reduction in energy consumption can be achieved [2].

Nevertheless, applying interior insulation is not without challenges since the hygrothermal conditions in the exterior wall also change. Outbound heat flow through the wall decreases, thereby lowering outward drying capacity, and the added interior insulation solution will by adding vapor resistance reduce inward drying. Hence, an interior insulated wall becomes more sensitive to moisture sources. This has instigated research focus on both how to protect from moisture sources and how to improve drying conditions, e.g., [3–7]. Problematic moisture sources are driving rain [3,8], leaks in the building envelope [4], rising moisture from the ground [9], and indoor humid air condensing in the wall where it meets the saturation temperature [6]. Protection from driving rain and leaks involves measures

such as improvement of rainproofing details, repairment of mortar joints, and provision of external render or hydrophobization. Protection from indoor humid air involves applying a vapor barrier or retarder, or ensuring low indoor relative humidity (RH). Sufficient protection may not easily be achieved for protected facades with strict limitations to external render and façade appearance. Ensuring a level of drying may, therefore, also be necessary. Strategies to improve drying include, for instance, applying capillary-active insulation materials, leaving a gap in insulation at beam ends, increasing temperature in beam ends, or utilizing smart vapor barriers (SVBs) or retarders (SVRs) that allow inward drying.

1.2. Hygrothermal Modeling

Designing case-specific solutions requires knowledge of the solution performance under realistic climate exposure or exposure to a design climate. Hygrothermal simulation has become a central tool for investigating such performance, e.g., [10,11]. Nevertheless, establishing realistic simulation models does not come without challenges. There are numerous complicating aspects related to establishing a model of masonry in hygrothermal simulation software. Overall, these aspects involve issues on how to model moisture sources, material properties, and the masonry to account for interaction between brick and mortar. Modeling moisture sources involves questions of rain distribution on façade, rain impact and runoff, rain absorption, and moisture infiltration [12–14]. Modeling material properties engages uncertainty regarding anisotropic behavior [15], moisture retention and hysteresis [16], moisture-dependent liquid conductivity [17–19], and vapor diffusivity, including uncertainty from lack of property measurements. Modeling masonry involves addressing complexity of material connectivity or interface resistance [20,21], material inhomogeneity, and changing properties along interface planes between brick and mortar [22,23], including moisture penetration and infiltration pathways [24], all dependent on mortar curing and curing moisture content, brick-and-mortar properties, and craftmanship during brick laying [25].

To further elaborate on the complexity regarding masonry performance and modeling of masonry, a selection of relevant research literature findings are summarized. Brocken [22] found moisture-transport properties of mortar joints to vary significantly. It was concluded that it was not possible to discern whether interfaces had perfect or imperfect hydraulic contact. Nevertheless, Brocken discovered that by shifting part of the retention curve for mortar to lower capillary pressures a simulation with perfect hydraulic contact would give reasonable results. Ramirez et al. [15] found resistance effects during absorption to be directionally dependent on materials, with most effect detected from lime mortar to brick, attributing it to discontinuity of the finer mortar pores. Whereas, in a drying experiment, Ramirez et al. [15] could not detect any resistance effects from the experiment results themselves. Zhou et al. [23] found no directional dependence for interface resistance. Instead, the resistance was found to be strongly dependent on local capillary pressure, and that relatively small changes in resistance value had large impact on moisture-distribution profiles. Vereecken and Roels [21] investigated simulation models in 2D with and without interface resistance and concluded that interface resistance had negligible impact when the wall was subjected to alternating wetting and drying from real weather, even though it had impact on a stand-alone imbibition process.

Hens [26] investigated vapor diffusion resistance in one-stone-thick masonry leaf specimens and found the resistance to be much lower than for the brick itself, attributing it to microcracks at the brick–mortar interface and imperfect joint filling. From the results presented by Hens, the vapor resistance decreased approximately to a third, although precise comparison is difficult due to a dependence on RH throughout the material. Similarly, Vereecken et al. [27] also reported lower vapor resistance of a masonry composite than for the individual brick and mortar constituents.

Gutland et al. [28] modeled fractures along brick–mortar interfaces as a material domain with hygrothermal properties derived from a fracture model. Their simulations demonstrated increased absorption from such modeling, and under cyclic conditions significantly increased drying compared to a base model without fracture(s).

Jensen et al. [6] ran numerical simulations, varying a range of parameters after an initial automated calibration of initial moisture content, rain-exposure coefficient, and shortwave-absorption coefficient. They found less RH fluctuation in the simulation than in the experiment and pointed to this seemingly being a common issue for simulation programs reported among other studies, and it could be related to not including hysteresis effects.

Johanson et al. [29], in a comparison between experiment and simulation, found the moisture progression to be considerably faster in the experiment than in the simulation.

Findings such as the aforementioned promote discussion on how to approach hygrothermal modeling of masonry to capture realistic performance.

1.3. Objective and Scope

The objective of the current study is to highlight uncertainty in hygrothermal simulation of an interior insulated brick wall, and to study impact of some modeling choices or simplifications, by addressing several influential aspects in simulation model setup and execution. Simulations are compared to a large-scale laboratory experiment of Knarud et al. [30] as a check of realism. However, it should be made clear that this is not a validation exercise. Nor is it a calibration study. Instead, it is a study highlighting modeling uncertainty and sensitivity to modeling choices, which is accompanied with some remarks on conservativeness in hygrothermal modeling.

The investigated object is an interior insulated masonry wall segment subjected to wetting and drying in a simple climatic sequence. It is insulated with mineral wool and fitted with a smart vapor barrier (SVB) to allow for inward drying. Detailed description is provided by Knarud et al. [30]. Nevertheless, central parts of the description are summarized in Section 2.

The exterior surface of the masonry consists of bare brick. It is therefore more complicated to investigate than masonry with external render. External render acts like a capillary retarder by creating a uniform layer that almost entirely removes the chance of moisture infiltration through brick-mortar interfaces. With a wall without external render, we however face many of issues of modeling masonry.

A common challenge with conducting hygrothermal simulations is incomplete available description of material properties when, for instance, it is not possible to completely map all the properties through laboratory testing and measurements. Complete mapping of properties is a very extensive and laborious process, that requires extensive effort, e.g., [16,31,32]. In addition, for in situ studies, identification of material properties is often limited to non-destructive measurements. Therefore, many simulation studies, e.g., [6,33,34], are conducted with some properties unknown, which are then substituted with properties from presumed similar materials. However, this inserts uncertainty.

With this in mind, the objective is approached by addressing three research questions:

1 When applying modelled hydraulic conductivity what are the consequences of uncertainty regarding the following material properties?
   - Capillary absorption coefficient;
   - Retention curve.

2 What impact do modeling choices or simplifications have on simulation results? Aspects that herein will be investigated are:
   - Reading position of results in simulation model compared to sensor location in physical experiment;
   - Isotropic vs. anisotropic wood properties for beam end;
   - Including increased permeability along the brick–mortar interface in mortar properties during rain events;

- Presence of a particularly "leaky" mortar joint, due to lower brick–mortar interface quality, and distance of such a joint to the sensor;
- 2D simplification compared to simulation in 3D.

3 What effect is seen from modeling a smart vapor barrier compared to no barrier or traditional barrier?

The main novelty follows research question 2 which is not a typical focus of similar studies. Although question 1, to some extent, has been investigated in other studies [19,35], these studies focus on much more limited geometric extents, not a masonry wall envelope. Regarding question 3, SVB has not previously been given much explicit focus, even though SVR has been included in simulation studies [36,37]. SVB contribution to inward drying has not been much reported on regarding masonry with beam ends.

Magnitude of observed sensitivity will, of course, depend on what is investigated, that is, the scenario that is being studied. Direct extrapolation of sensitivity results from one studied scenario to other scenarios is, thus, challenging. Therefore, actual quantification of sensitivity will not be provided other than visual demonstration of the impact on results.

Other limitations: Rainwater runoff, splashing, and surface adherence will not be addressed. Instead, the modeling approach is simplified to seek the maximum rain absorption that the rain load and material properties allow for. Wetting of the masonry is, therefore, approached in a form of worst-case scenario; although, this does not exclude localized infiltration through leak points (interpenetration) being able to create even more severe wetting. Transverse interface resistances, between brick and mortar, that allows for impeded moisture absorption across collar joints and between bricks and bed joints in the masonry are neither included nor addressed. With the exception of retention curve and hydraulic conductivity, only average values are used for material properties involved, i.e., the sensitivity of property variability is not extensively investigated.

A question arises as to whether simulations become realistic, with strong replicability of laboratory results or conservative, providing an "on-the-safe-side" enveloping result which laboratory results are not worse than.

The present work aims to investigate the influence or sensitivity of modeling choices on results, in contrast to a traditional sensitivity analysis that samples values of properties or boundary coefficients from probability distributions. The aim is also to approach perspectives on conservativeness in modeling.

2. Case Study Description—Materials and Methods

2.1. General

The masonry structure is part of a larger experimental study of nine differently composed wall segments shown in Figure 1a. A detailed description of the experiment can be found in [30]. Of the nine segments, the current paper will address simulation of segment 4, which has 50 mm glass-wool insulation and SVB. Segments 2, 5, and 6, which all have the same brick type and masonry thickness as segment 4, will also briefly be mentioned or addressed for comparison. Each segment includes a wooden beam end inserted into a beam-end pocket in the masonry. Segments 4 and 6 are equipped with SVB while segment 5 has polyethylene vapor barrier. The wall is exposed to an exterior climate sequence ensuring first wetting of the wall through cold-climate rain events before ensuring drying in relatively warm climate conditions. The following subsections will in brief describe the masonry materials, interior structure, instrumentation, experiment setup, and climatic sequence. For more details refer to [30].

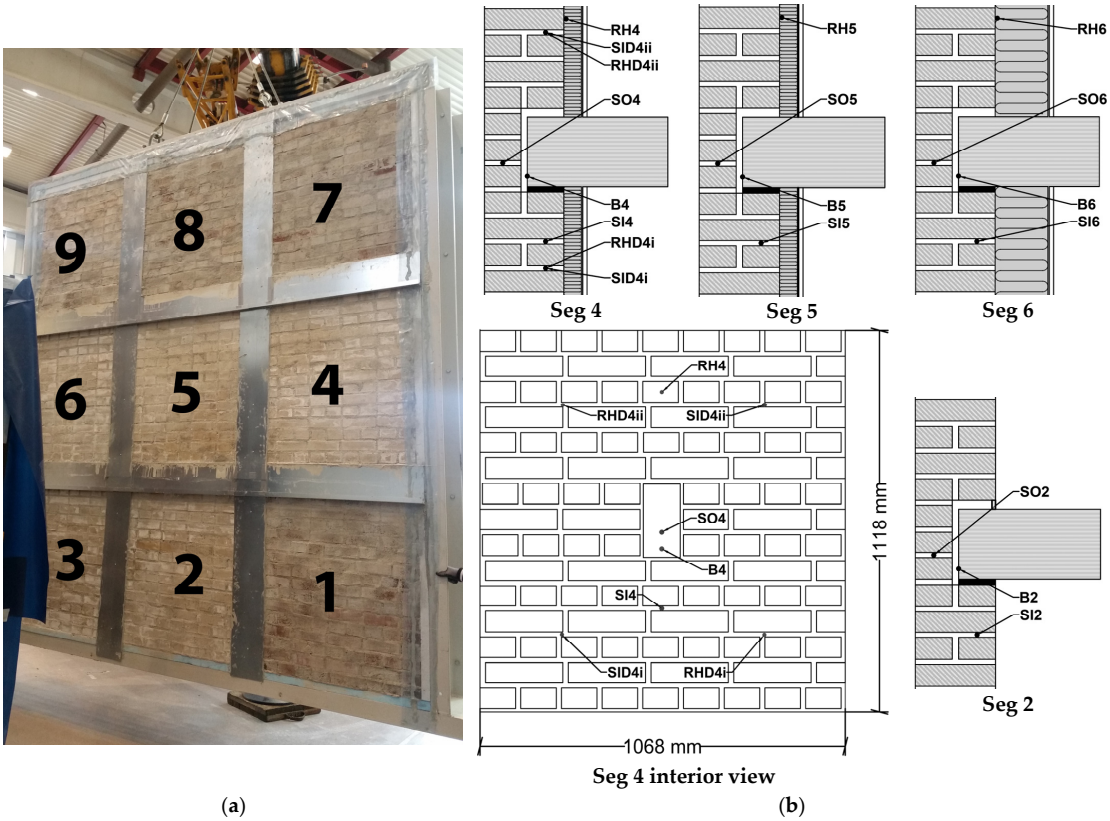

Figure 1. Test wall. (**a**) Exterior face with flashings/gutters mounted. Each segment numbered. (**b**) Cross-sectional overview of the four wall segments, including sensor locations.

2.2. Masonry Materials

The brick (Figure 2) used for the addressed segments is a high-initial-rate-of-absorption (IRA) brick, which is presumed to be close in performance to typical bricks found in older buildings (late-19th to mid-20th century) [30]. The mortar is a prescribed LC-mortar; LC 50/50/610, where the numbers correspond to lime/cement/aggregate mass ratios of binder content. Material properties, masonry dimensions, and masonry construction are further described in [30]. Property values applied in the simulation model are listed in Appendix A, with further description of hydraulic conductivity in Section 4.1.

Figure 2. Close-up of bricks during brick laying.

2.3. Interior Structure

The interior structure of segment 4 consists of 50 mm interior glass-wool insulation (0.034 W/(m·K) thermal conductivity), a SVB, and an interior finish of 13 mm gypsum board. The SVB vapor-resistance properties applied in the simulation model are discussed and described in detail in Appendix B. Segments 5 and 6 are the same as segment 4 except,

respectively, having a traditional polyethylene vapor barrier ($s_d \approx 50$ m) instead of a SVB and 150 mm insulation instead of 50 mm. Segment 2 has no interior structure and acted as a reference in [30]. A spruce beam end, 400 mm long, 107 mm wide and 213 mm high, is placed in the beam-end pocket on an asphalt sill gasket. There is a 10–20 mm gap between the pocket rear end and the beam end (18 mm in simulation model). The transition between beam end and vapor barrier is rendered vapor- and airtight.

2.4. Instrumentation

A number of Sahlen sensors (SO, SI, and SID), RH sensors (RH and RHD) and beam-end wood moisture electrodes (resistance moisture meters) (B) are located in the structure, as shown in Figure 1b. However, for the current paper, only RH4–RH6 and B2, B4–B6 are addressed. For more information, refer to [30].

2.5. Experiment Setup and Climate Sequence

The wall segments were tested in a large-scale building envelope climate simulator. This simulator contains both an exterior and interior climate chamber. On the exterior, the wall was exposed to dynamic conditions following a climate sequence provided in Figure 3b, whereas on the interior, the conditions were kept constant after initial conditioning, see Figure 3a. First, the wall was exposed to a cold exterior climate including four pairs of rain events (2 × 10 min, 2 × 20 min, 2 × 40 min, and 2 × 40 min), constituting a "wetting period", before it was exposed to a warm climate, constituting a "drying period". The rain exposure had a magnitude of constant 47 mm/h which is relatively high when compared to relevant real-world rain intensities [30]. The purpose of the climate sequence was to observe and compare rate of wetting and subsequent drying in differently constructed masonry wall segments, with focus on SVB and beam-end performance in this regard. A more detailed list of the climate sequence can be found in [30]. The same climate sequence was applied in the simulation model.

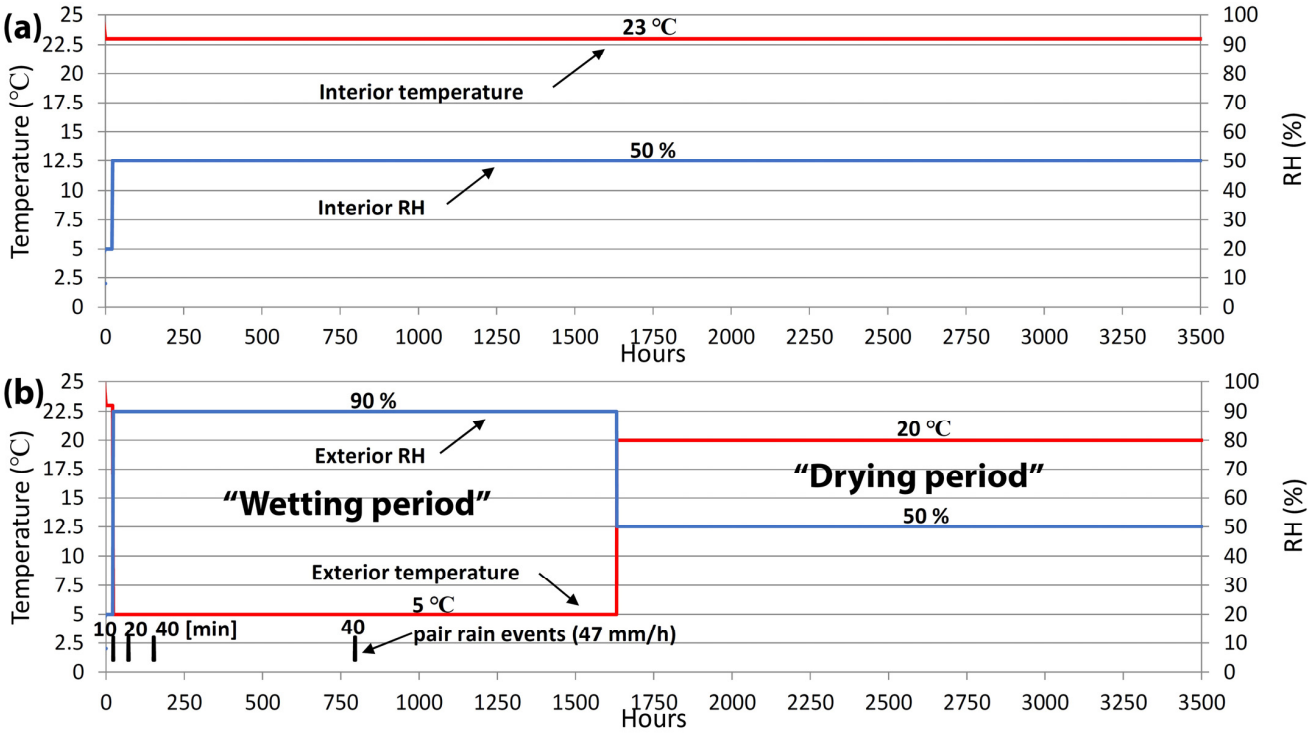

Figure 3. Climate sequence overview; (**a**) interior climate and (**b**) exterior climate. Reproduced from [30].

3. Hygrothermal Modeling

3.1. Model Physics

A model was set up to simulate the experiment scenario. The hygrothermal simulation model is an in-house physics model set up in COMSOL Multiphysics [38]. COMSOL provides a physics model builder, in the form of partial differential equations (PDEs), which were utilized in the current study to describe the balance and transport equations for moisture and heat. Furthermore, COMSOL includes numerical solvers based on the finite element method (FEM), of which the PARDISO (parallel sparse direct solver) has been employed. Previous versions of the model physics were applied in [39,40], with the current version having been developed further from these to better handle heavy rain exposure as a boundary condition. Furthermore, handling of the specific moisture capacity was corrected for non-isothermal conditions. That is, [39,40], unfortunately, did not include the temperature differential of the capillary pressure in connection to the specific moisture capacity, see Equation (1), which was the cause of the daily fluctuations experienced in benchmark 1 in [39]. The current version was also improved to more realistically represent the sorption/retention in both the hygroscopic and over-hygroscopic regions, see Equation (A1) Appendix A. Since the retention curve consists of two parts, the first part being dependent on RH (hygroscopic region) and the second part dependent on capillary pressure (over-hygroscopic region), the specific moisture capacity was split into two terms, $dw_\phi/d\phi$ and dw_{pc}/dp_c, in Equation (1).

$$\frac{dw}{dt} = \frac{d}{dt}\left(w_\phi + w_{p_c}\right) = \frac{dw_\phi}{d\phi}\frac{d\phi}{dt} + \frac{dw_{p_c}}{dp_c}\frac{dp_c}{dt} \tag{1}$$

where w is moisture content [kg/m^3], w_ϕ is the moisture retention curve term for hygroscopic region, w_{pc} is the moisture retention curve term for over-hygroscopic region, t [s] time, ϕ [-] RH, p_c [Pa] capillary pressure, and where the time-derivative of the capillary pressure is expanded as:

$$\frac{dp_c}{dt} = \frac{dp_c}{d\phi}\frac{d\phi}{dt} + \frac{dp_c}{dT}\frac{dT}{dt}$$

where T [K] is temperature.

The moisture balance is given by Equation (2), which originate from equivalent expressions derived in [41,42]. Since the scenario studied does not contain air transport, vapor transport due to air diffusion (or convection) is not included.

$$\frac{dw}{dt} = \frac{d}{dx_j}\left(\left[\delta_v P_{sat} + D_\phi\right]\frac{d\phi}{dx_j} + \left[\delta_v\phi\frac{dP_{sat}}{dT} + D_\phi\frac{\phi}{T}ln(\phi)\right]\frac{dT}{dx_j} + \frac{D_\phi}{R_w}\frac{\phi}{T}g\cdot\vec{e_z}\right) \tag{2}$$

where δ_v [kg/(m·s·Pa)] is vapor diffusivity, P_{sat} [Pa] saturation pressure, D_ϕ [kg/(m·s)] capillary diffusivity for ϕ as driving potential ($D_\phi = K\rho_w R_w T\phi^{-1}$), K [s] hydraulic conductivity, ρ_w [kg/m^3] water density, R_w [J/(kg·K)] specific gas constant for water vapor, g [m/s^2] gravity, and e_z unit vector for z-dimension (dimension of acting gravity, positive in the opposite direction to that of gravity).

The enthalpy balance is given by Equation (3), when omitting the contribution from change in air content and humid air vapor content in the pore structure. A similar expression is derived in [43].

$$\begin{aligned}\rho_s c_{p,eff}\frac{dT}{dt} &= \frac{d}{dx_j}\left(\left[\lambda_{eff} + h_{vap}\delta_v\phi\frac{dP_{sat}}{dT}\right]\frac{dT}{dx_j} + h_{vap}\delta_v P_{sat}\frac{d\phi}{dx_j}\right)\\ &+ D_\phi\left(\frac{d\phi}{dx_j} + \frac{1}{R_w}\frac{\phi}{T}g\cdot\vec{e_z}\right)c_{pw}\frac{dT}{dx_j}\end{aligned} \tag{3}$$

where ρ_s [kg/m^3] is the density of solid material, $c_{p,eff}$ [J/(kg·K)] effective heat capacity ($c_{p,eff} = c_{ps} + c_{pw}w/\rho_s$), c_{ps} and c_{pw} specific heat capacity of solid dry material and liquid water, respectively, λ_{eff} [W/(m·K)] moisture-dependent effective thermal conductivity

(temperature dependence is omitted), and h_{vap} [J/kg] specific enthalpy of evaporation (temperature dependent).

The rain boundary moisture flux is modeled as an approximation to Equation (4) [44].

$$g_{l,eff} = min\left[g_l, K_{c,cap}\frac{dp_c}{dx}\right] \quad (4)$$

where $g_{l,eff}$ and g_l [kg/(m^2·s)] are, respectively, effective boundary moisture flux and actual rain flux, and $K_{c,cap}$ [s] capillary conductivity at capillary saturation.

The approximation to Equation (4) is given by Equation (5).

$$g_{l,eff} = min\left[g_l, -D_{\phi,cap}\left(\frac{\phi - \phi_{acc}}{b_{l,min}} + ln\phi\frac{\phi}{T}\frac{T - T_e}{b_{l,min}}\right)\right] \quad (5)$$

where $D_{\phi,cap}$ is D_ϕ at capillary saturation, ϕ and ϕ_{acc}, respectively, RH of the first boundary cell and of an arbitrary set RH accuracy level assumed for moisture film at boundary (ϕ_{acc} = 0.99999, equivalent to p_c = 1351 Pa at 20 °C, well below capillary saturation of the retention curves), $b_{l,min}$ [m] thickness of the first and thinnest boundary layer cell at the exterior boundary surface (arbitrarily set to $b_{l,min}$ = 0.0005 m), and T and T_e [K], respectively, temperature of the first boundary cell and exterior temperature.

Not using Equation (5) in combination with boundary layers, but instead limiting moisture uptake on saturation only, can provide marginally higher moisture uptake. However, the fine meshing that boundary layers provide is believed to give a more accurate account of moisture content and absorption conditions at the exterior surface. Still, this issue has not been investigated extensively in the present study, and uncertainty thereby persist regarding whether the approach chosen is the most optimal approach. A relevant model algorithm validation by benchmarking is documented in Appendix C.

3.2. Limitations

There are some limitations to the model due to lack of certain information:

1. With material property data mostly available for one direction only, materials are, in general, modeled as isotropic;
2. Moisture retention and capillary conductivity as functions of capillary pressure have not been tested for in the current study. Approximate guesstimates have instead been applied, based on the materials' sorption curves and capillary absorption coefficients, and retention curves of what are believed to be similar materials;
3. Interface resistances between materials are not included, i.e., the model assumes full hydraulic contact;
4. Hysteresis has not been included. Materials are only modeled on adsorption and absorption data.

Consequences of 1.: the isotropic simplification will especially affect the bricks and the mortar joints. The spruce beam end is modelled anisotropic as default. For the bricks, the capillary transport coefficient has been measured through the brick face, which for these bricks is the surface with the finest pore structure and, presumably, the side with the highest resistance to water penetration. The brick head has similar appearance. Higher capillary transport coefficients could be expected in other directions, i.e., moisture absorption through the brick bed or stretcher (opposite face). Larger pores and cracks can especially be seen on the brick bed. Since the rain moisture exposure is one-directional with a combination of brick face and head being exposed, both the bed and stretcher directions are, presumably, less important; however, bed absorption would be important if the model were to explicitly replicate additional influx of moisture along the brick–mortar interface. More information about the specific modeling is provided in Section 3.4.

Regarding 2.: not having the exact retention and capillary conductivity curves as functions of capillary pressure for the masonry materials in question is inconvenient for a simulation case which is so heavily determined by capillary transport during and after rain

absorption. Having adequately described retention and capillary conductivity functions is essential for arriving at high confidence simulation results. However, since such functions are not available for the specific materials in this study the functions had to be established from the material data being available (sorption curves in hygroscopic region and capillary absorption coefficients), together with retention curves of similar materials described in the research literature. Descriptions and details regarding applied material property functions are given in Appendix A and displayed in Sections 4.1 and 4.2.

Concerning 3.: interface resistances between different materials can significantly influence moisture transport in masonry [23], i.e., impede moisture movement between materials during absorption and redistribution conditions. Thus, not including them will allow faster moisture transport across the masonry than the actual situation. However, it can also result in different moisture distribution in the masonry compared to reality [23]. During drying conditions, insignificant influence from not including interface resistance is expected, see [15].

As for 4.: not including hysteresis is a common simplification due to the complexity of hysteresis modeling and extensiveness of required material testing. However, not including hysteresis will inherently cause uncertainty.

3.3. Key Uncertainty Regarding Material Properties

In the present study, not all material properties are available for the specific brick and mortar applied in the experiment. Basically, it was not possible within the extent of the experiment in [30] to fully measure all properties, due to limitations in laboratory resources and time. Table 1 provides an overview of necessary material properties and how they have been determined for the hygrothermal simulation. Key properties, such as the moisture retention and hydraulic conductivity ([35]), have not been measured but were taken from perceived similar materials and modelled, respectively, where, in addition, modeling of the hydraulic conductivity requires the moisture retention as input [17]. Significant uncertainties are, therefore, introduced. This provides an ample example to demonstrate typical uncertainty challenges hygrothermal simulation efforts encounter due to limited resources for complete mapping of properties. Impact of this uncertainty will be further addressed in Sections 4.1 and 4.2.

Table 1. Necessary material properties, including partial or indirect properties for the retention and hydraulic conductivity. Includes overview of determination: measured (Mea.), from standard (Sta.), from similar materials (Sim), modelled (Mod.), and estimated (Est.).

	Storage	**Determination**	**Transport**	**Determination**
General	Density, ρ_s	Mea.		
Heat	Specific heat capacity, c_p	Sta.	Thermal conductivity, λ	Sta. (dry), Sim. (wet)
Moisture	Sorption (hygroscopic), $w(\phi)$	Mea.	Vapor diffusivity, δ_v	Mea.
	Retention (over-hygroscopic), $w(p_c)$	Sim.	Hydraulic conductivity, $K(p_c)$	Mod.
	Capillary moisture content, w_{cap}	Mea. (brick)/Mea. Sim. (mortar)	Capillary absorption coefficient, A_w	Mea. (brick)/Mea. Sim. (mortar)
	Saturated moisture content, w_{sat}	Est. Sim.		

3.4. Simulation Model Design Setup

Illustration of the overall 2D model is provided in Figure 4a, where different colors indicate different materials. The model lumps the additional moisture influx along the brick–mortar interface together with that of the mortar as a simplification and, thereby, ends up with an increased capillary conductivity for the mortar during absorption. That is, lumped properties are applied only during rain events. Figure 4b illustrates how the mortar joints are modelled. Joints with a continuous brick–mortar interface from the exterior are modeled with the lumped properties (dark blue Figure 4b). Whereas mortar joints that have no brick–mortar interface continuity to the exterior are modeled with normal mortar properties (light blue–grey Figure 4b). The mortar with lumped properties arrives at a

capillary absorption coefficient in the same order of magnitude as the brick, see Appendix A.

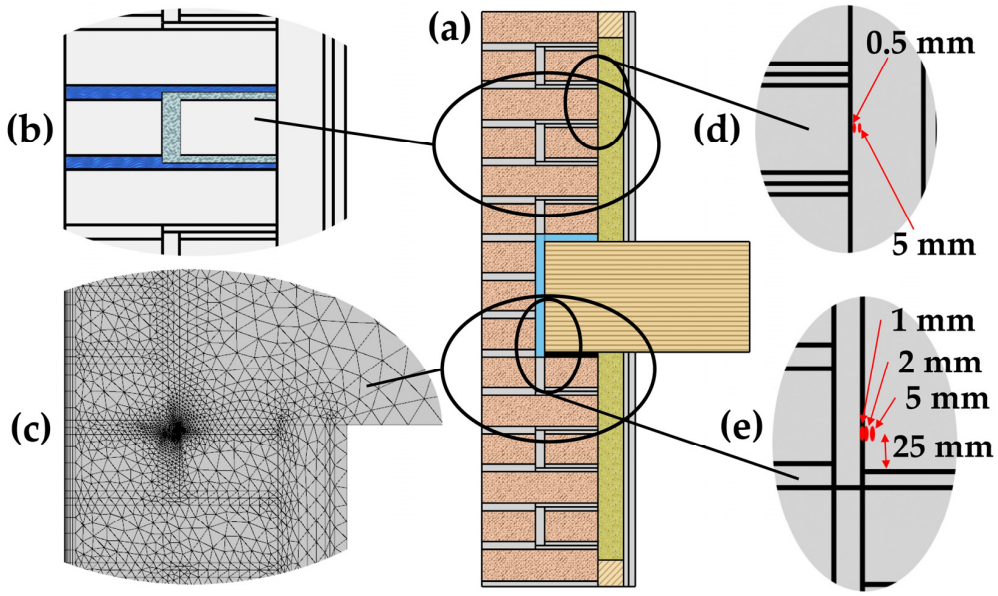

Figure 4. (**a**) Overview of simulation model. (**b**) Joint modeled in two zones; one continuous (dark blue), capturing the uninterrupted brick–mortar interface traversing the wall; the other (light blue–grey) capturing the collar joint and the mortar not having continuous interface from the exterior. (**c**) Illustration of applied mesh resolution. Reading position distances of simulation results at: (**d**) the interior of the masonry; and (**e**) the beam end.

The air cavity around the beam end is modeled as humid air according to formulas in [45], corrected for radiation and convection over a cavity width of 20 mm following the WUFI help file [46]. However, for simplicity it is only corrected for as a vertical cavity in the transverse direction; thus, neither accurate for the horizontal cavity-part above the beam end, nor correct in the vertical direction for the vertical cavity.

Description of how the SVB is modelled is provided in Appendix B.

The exterior and interior heat-transfer coefficients are both taken as 25 W/(m^2·K), whereas the vapor-transfer coefficients are both 2×10^{-7} s/m. Equal coefficients are used on both sides due to the ventilation conditions created by the climate simulator.

Model boundary conditions are given a timestep resolution of 600 s to capture the climate sequence of the experiment. The simulation is run with maximum timesteps of 30 s for rain events and the temperature jump (Figure 3) and the 20 min leading up to the events. For the temperature jump, small timesteps are applied to accommodate model algorithms of the humid air layer behind the beam end. Otherwise, temperature jumps would not be a particular issue requiring low timesteps. Timesteps of 600 s are used for approximately 2 h prior to boundary condition changes. Elsewhere, timesteps of 3600 s are used. Low timesteps in the lead-up time to events or boundary condition changes is a technical measure taken to avoid timesteps having been shifted to the point where they overstep events, which can happen in COMSOL when using free time-stepping taken by the solver in combination with maximum step size, since it only updates timestep size before initiating a new timestep. Thus, if operating with, for instance, timesteps of 600 s or 3600 s up to an event one might risk losing, respectively, up to almost 600 s or 3600 s of the event. Before this became apparent to the authors, some simulation try runs lost a rain event causing strange inconsistency between results.

Applied mesh resolution is illustrated in Figure 4c. Increasing mesh resolution further did not provide significant impact to results. The mesh includes eight boundary layers on the exterior surface that is exposed to driving rain. The thickness of the layers grows with a stretching factor of 1.3, with the outermost, and thinnest, being 0.5 mm thick. The high mesh resolution below the corner of the beam end is due to the humid air at a point in time reaches saturation and condensation conditions when in contact with the asphalt sill gasket. However, surface condensation from humid air is not included in the model. Instead, the humid air is allowed to go to unphysical supersaturation. This simplification was deemed acceptable since these conditions only happen at this location for some hours after the temperature jump initiating the warm period.

4. Results and Assessments

If not otherwise stated, the RH reading position is taken 5 mm from the interior masonry surface, and the beam-end moisture content reading is taken 2 mm into the beam end 25 mm from the bottom, see Figure 4d,e.

Note that the resistance moisture meters used to detect moisture content in the beam ends did not manage to provide reliable moisture contents below 8–10%. Furthermore, in the experiment the acclimatization time from very dry conditions was insufficient to arrive at consistent 20% RH throughout the structures. Hence, the sensors display lower RH and moisture content than the initial condition used in simulations, with the latter following the exterior and interior climate at the experiment onset. The initial conditions of the experiment and the simulations are therefore not comparable. The consequence of this should, nevertheless, be insignificant after moisture from rain events reaches the sensors or reading positions.

4.1. Uncertainty from Hydraulic Conductivity

Hydraulic-conductivity curves are modelled following a bundle-of-tubes model described in Knarud et al. [17]. Input to generate a conductivity curve includes A_w-value, retention curve, and vapor resistance. Among these inputs, uncertainty regarding impact of the A_w-value and retention curve will be assessed in this and the next section. For the brick, the A_w-value was measured [30] for enough specimens to identify standard deviation. Simulations with conductivity values generated for −2, −1, +1, and +2 std. of the A_w-value can, thereby, be assessed. Standard deviation was not given for mortar. Instead, a likely min–max range was provided. For simplicity, we here put the min as −2 std. and max as +2 std. so that hydraulic-conductivity curves can be generated in the same format for the two materials, see Figure 5a,b. As seen from Figure 6, the variation in A_w-value has a large impact on how early the RH sensor responds to increased moisture intrusion in the wall structure. The variation in mortar properties and, especially, in the lumped properties due to the large uncertainty span in A_w-values is likely a large contributor to this, whereas the variation for brick is likely of relatively low impact due to the low standard deviation for the brick. Interestingly, higher A_w-values do not increase RH in the warm period much, whereas lower A_w-values decrease the RH. This is due to changes in the saturation level at the masonry interior, where the higher A_w-values provide lasting ~100% RH at the masonry interior while lower A_w-values provide lower RH values. This reveals a downside with the conservative model setup, where little to no variation in RH reading value is possible upwards after the interior masonry reaches ~100% RH. Thus, impact of worsening material and model conditions falls into a blind spot of the RH sensor. What is left to be distinguished from the RH readings is the response rate to rain events in the first half of the cold period.

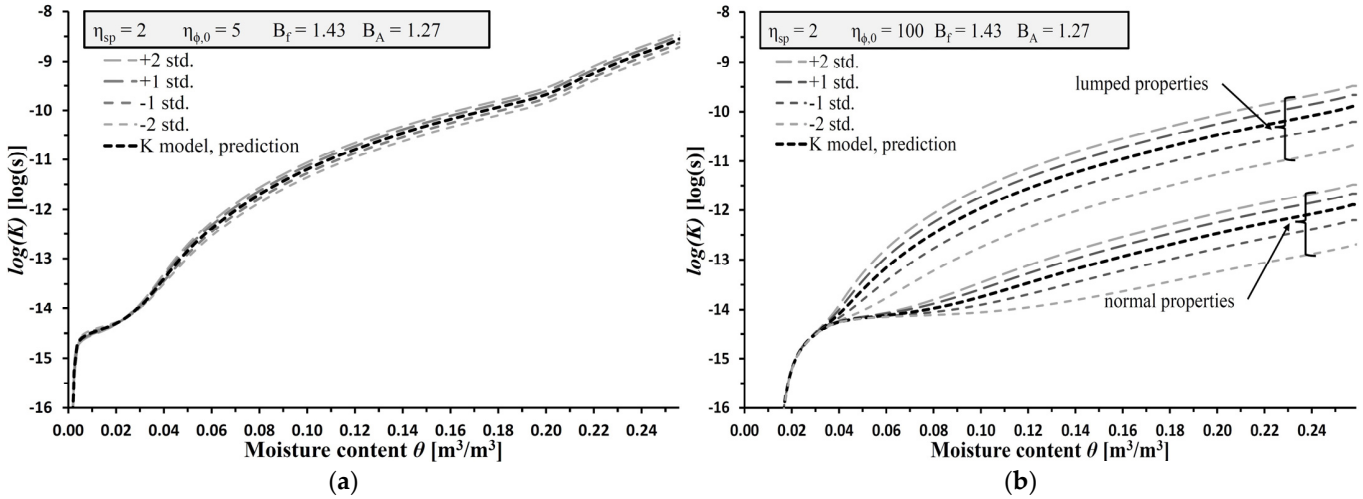

Figure 5. Uncertainty regarding hydraulic-conductivity curves modeled according to [17] based on standard deviation in A_W-value [30] for (**a**) brick and (**b**) mortar. Standard deviation for the mortar is unknown; however, ±2 std. is presumed to approximately correspond to the min–max range listed in [30]. Lumped properties are explained in Section 3.4 and Appendix A.

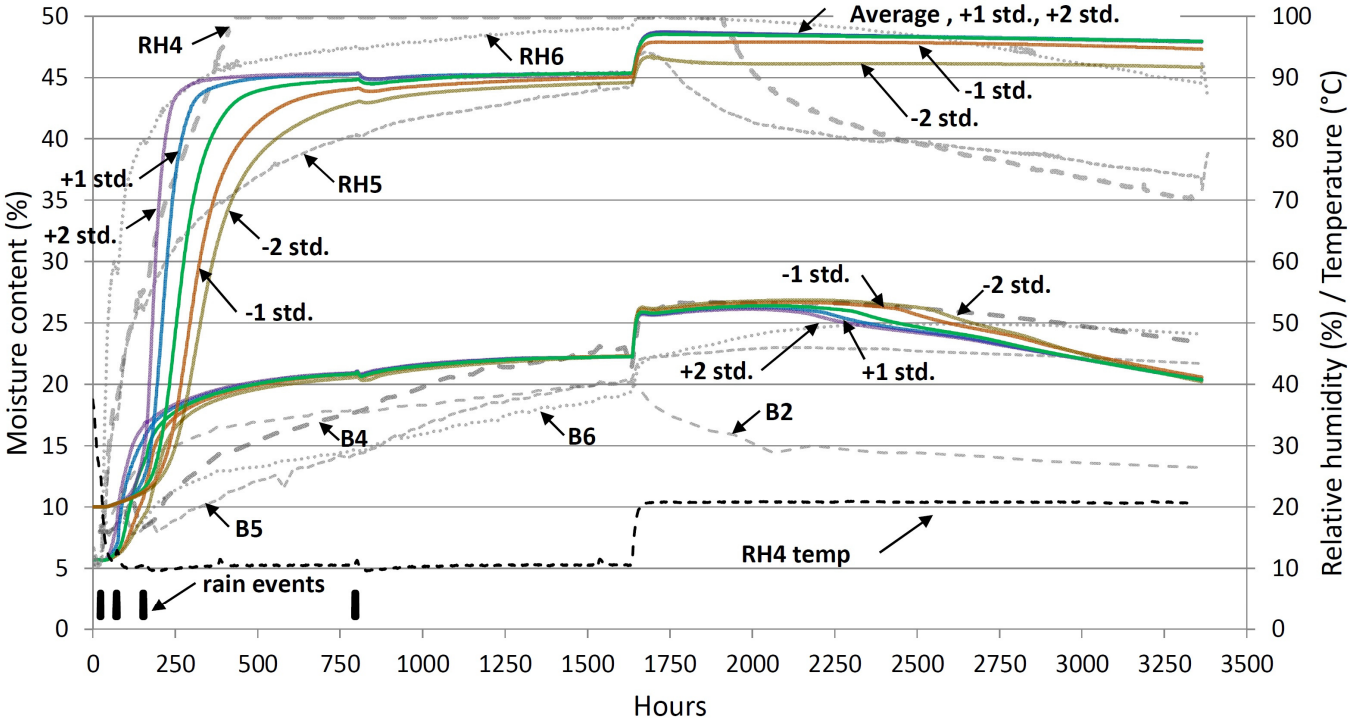

Figure 6. Result sensitivity to distribution range of A_W-values. Colored lines (green, default setup) provide RH and B simulated readings for seg. 4. Light grey dashed curves show results gathered in experiment (the same is the case in subsequent graphs showing results). Moisture content in weight-%.

For the beam end, higher conductivity curves provide earlier drying, while lower curves delay drying.

4.2. Uncertainty from Retention Curve

Regarding the uncertainty caused by not knowing the exact retention curve for the brick and mortar, impact of the retention curve is assessed. Uncertainty in the retention curve is approached by generating two extreme retention curve-"outliers", Figure 7a,c. The min- and max-retention curves, respectively, correspond to the perceived low and high end of pore sizes that are plausible for the materials. Associated hydraulic conductivity is generated with these retention curves, thus, giving corresponding min and max conductivity curves in Figure 7b,d. However, the lumped hydraulic-conductivity curve is taken as the default lumped-properties curve in Figure 5. The results, see Figure 8, display remarkably small difference between the simulations. The max setup has marginally earlier response and higher values for the RH reading, whereas the opposite is the case for the low setup. For the beam-end moisture content, the max and low setups provide, respectively, somewhat higher and lower moisture content at the onset of the warm period.

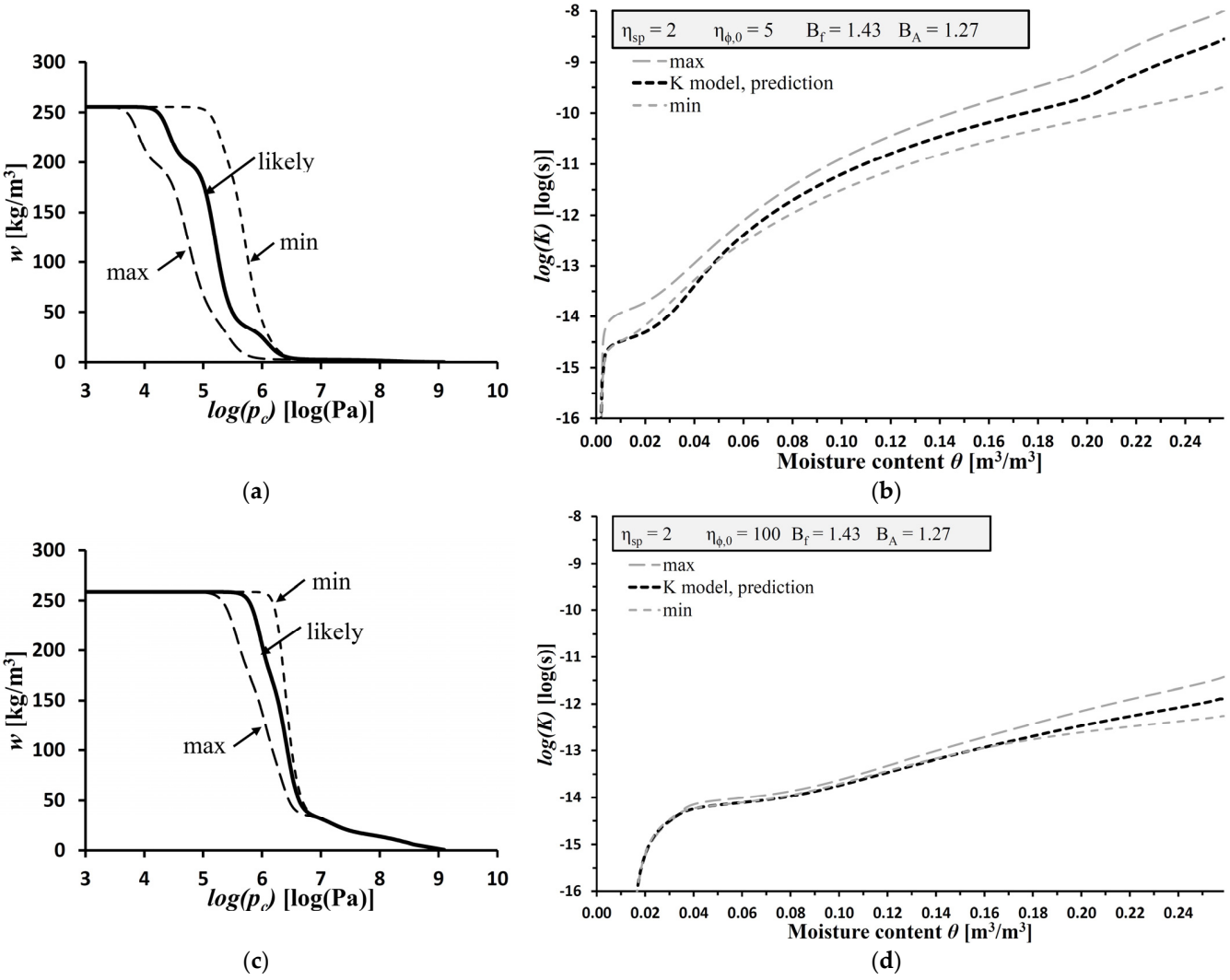

Figure 7. Variation in retention curves (**a**,**c**) to perceived outlying min/max limits, including change in hydraulic-conductivity curves (**b**,**d**), respectively, for (**a**,**b**) brick and (**c**,**d**) mortar.

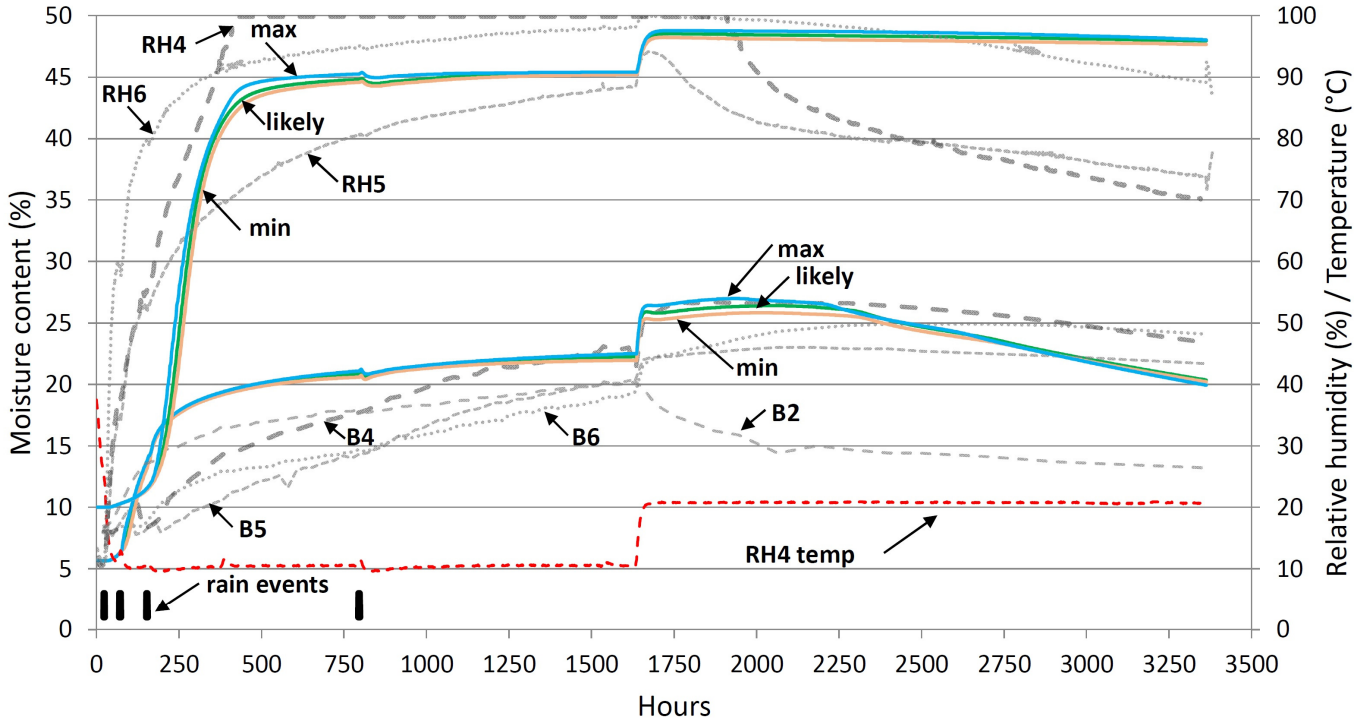

Figure 8. Sensitivity of variation in retention curves.

4.3. Reading Position

Initially, the RH reading position was assumed to align with the center of the RH sensor. With the sensor having a thickness of approximately 10 mm, the reading position in the simulation model was taken 5 mm from the masonry interior surface. However, after reconsideration, this assumption was drawn into some doubt. Especially, since the simulation results, see Figure 6, seem unable to increase the RH much above 90% in the cold period at 5 mm distance, whereas RH 4 is seen to go higher. The result difference in Figure 9 follows closely the temperature difference between 5 mm and 0.5 mm (Figure 10), correlated with the consequent temperature-dependent change in saturated vapor pressure. Assessing the situation, the simulation model is simply built up with insulation in the location of the sensor, whereas in the experiment the insulation bends around the sensor. Hence, locating the reading position at a certain distance from the masonry will effectively put it into the insulation. Even though the glass wool is rather vapor-open, the insulation still provides a thermal resistance over 5 mm, which affects effective temperature and, consequently, the RH level. Also, it might be that the RH sensor is more sensitive towards the highest RH level one side of it experiences, that is, with one side being pressed up against the masonry, higher RH may be experienced at the RH sensor openings at that side, and, effectively, influence what is measured. In Figure 9, assessing the simulation results against the experiment, a 0.5 mm distance is closer to RH4 and RH6, while 5 mm distance is partly closer to RH5 in the cold period of the experiment. However, the higher RH6 curve can be partially explained with the increased insulation thickness (150 mm) causing the RH sensor to be in colder surroundings. The jump of the RH5 curve at the start of the warm period is also seen from the simulation with 5 mm distance.

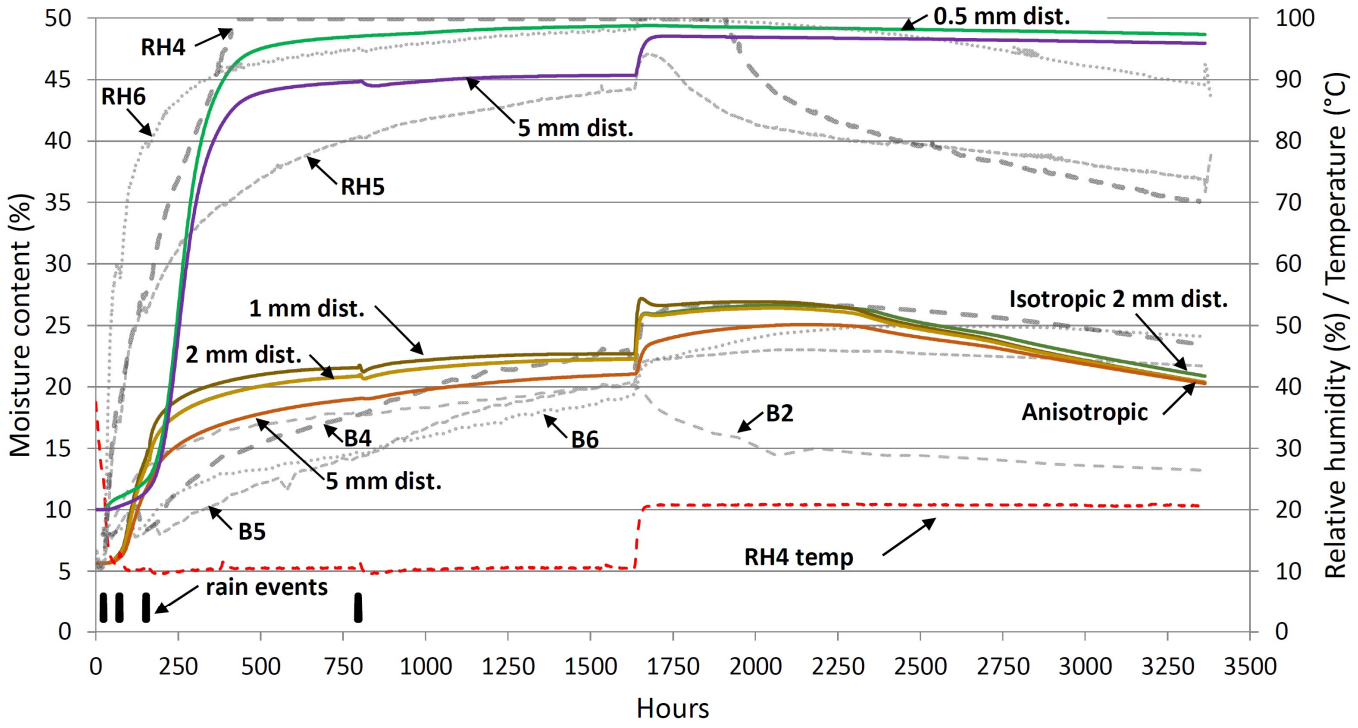

Figure 9. RH results for varying the reading-point distance from the interior masonry surface. Beam-end results for reading position, and isotropic and anisotropic beam-end properties.

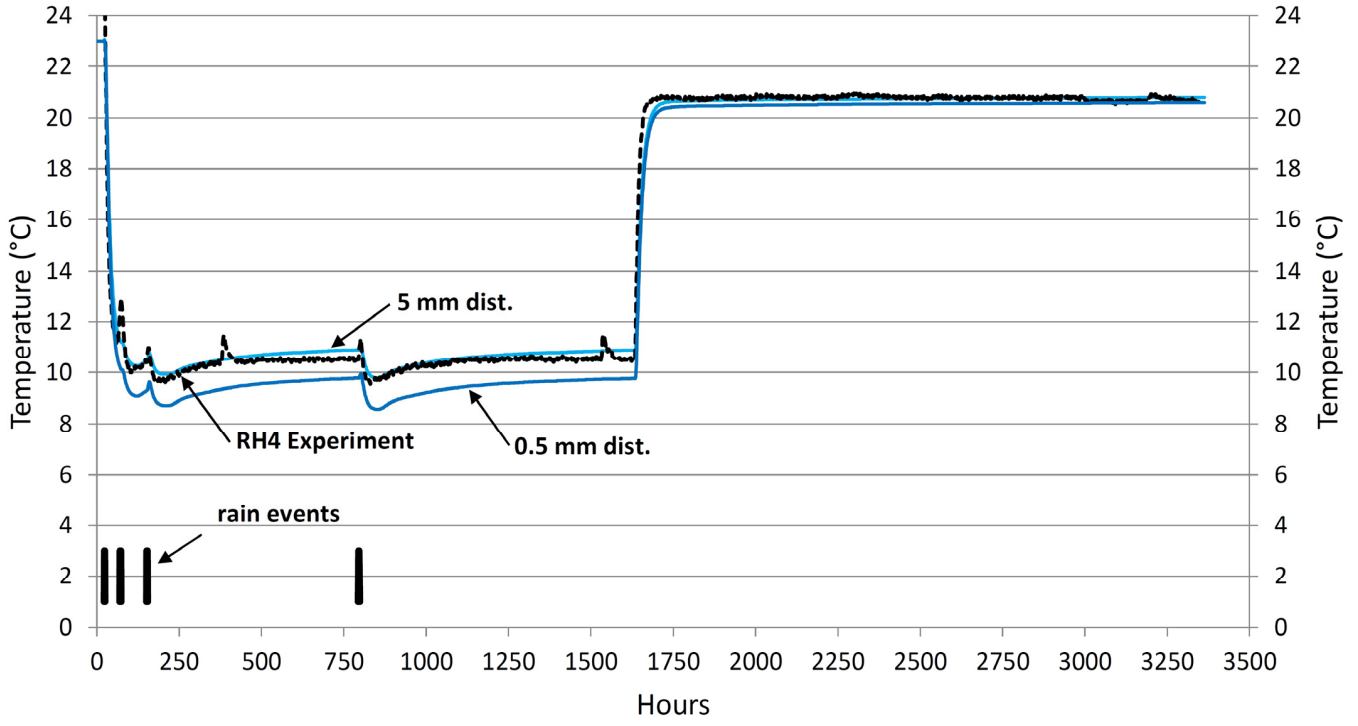

Figure 10. Temperature results. Varying reading-point distance from the interior masonry surface compared to experiment results of RH4.

Temperature reading at 0.5 mm is approximately 1.10 K lower than at 5 mm during the cold period (Figure 10), where the latter is almost a match to the measurement, but incrementally higher and lower during the cold and warm periods, respectively. Temperature peaks not aligning with rain events in the experiment results are likely due to ice

accumulation and defrosting of the ventilation system in the climate simulator. In perspective, specifically addressing the cold period, both results are, respectively, well within or at the ±1 K threshold for narrower accuracy range for at least 95% of the data, suggested by Huerto-Cardenas et al. [10] for model validation. However, the strictness of such a criterion is dependent on the variation in boundary temperature, and the criterion is intended for simulation in comparison to in situ or field measurement, not a laboratory climate sequence as is the case here. From these results, see Figure 10, it is indicated that choosing a RH reading position at 0.5 mm likely underestimates the temperature and overestimates the RH somewhat during the cold period.

Beam-end moisture readings are taken at 1, 2, and 5 mm into the wood, see Figure 4e. The readings at 1 and 2 mm are close to enveloping the B4 result in the cold period and the beginning of the warm period, whereas the moisture content decreases much faster than in the experiment over the second half of the warm period. The reading at 5 mm fails to be conservative for B4; however, it succeeds in being conservative for B5 and B6 for the cold period and the beginning of the warm period. It is relatively close in following the B2 trend over the cold period. There might be a significant uncertainty regarding the electric conductivity in the wood at these depths at the beam end, as it is affected by surface roughness, cracks, and local wood density and wood ring structure. Thus, local differences in wood structure can, by contributing to measurement uncertainty, explain the large differences between the segments, in addition to uncertainty regarding masonry heterogeneity and unevenness in the air-layer thickness, which affect moisture transport, that is.

4.4. Isotropic vs. Anisotropic Beam End

Applying isotropic material properties is a common simplification in hygrothermal modeling. It is, therefore, of interest to investigate the difference arising from such a simplification. For the isotropic case, longitudinal wood properties are used in both directions. In the anisotropic case, the wood properties in the vertical direction were replaced with radial properties for capillary conductivity and with twice the vapor resistance of the longitudinal direction, instead of the radial vapor resistance; this, with the assumption that the radial vapor resistance would be too strict considering the presence of cracks and the tangential influence in the 3D wood structure not being captured well by the 2D model. A difference between isotropic and anisotropic modeling is, indeed, seen in Figure 9, although not large. With the isotropic simulation, there seems to be a greater influx of moisture into the beam end from the masonry in the vertical direction, due to longitudinal wood properties, thereby, maintaining a higher moisture content longer than for the anisotropic simulation.

4.5. Effect of Lumping Mortar Properties and Brick–Mortar Interface Properties

A simulation was also undertaken with normal mortar properties for all joints, not compensating for the brick–mortar interface. An issue of numerical instability was experienced with this simulation at the fourth rain event (second rain event pair), preventing the simulation to proceed at acceptable speed. The instability is believed to have been caused by the mesh boundary layer, presumably, due to the large difference in capillary conductivity between mortar and brick along these layers. The solution became to replace the exterior 5 mm of the mortar joint with mortar having lumped properties. The mesh boundary layer was reduced to six layers with growth governed by a stretching factor of 1.1, and joints in the exterior half of the masonry were given increased mesh resolution for smoother transition from the boundary layers. This ensured that boundary layers would be well within the exterior 5 mm of the joints. Boundary layers were kept, due to Equation (5).

As seen in Figure 11 the simulation with normal mortar property joints results in both a later RH curve in response to rain events and a lower curve for beam-end moisture content during the warm period.

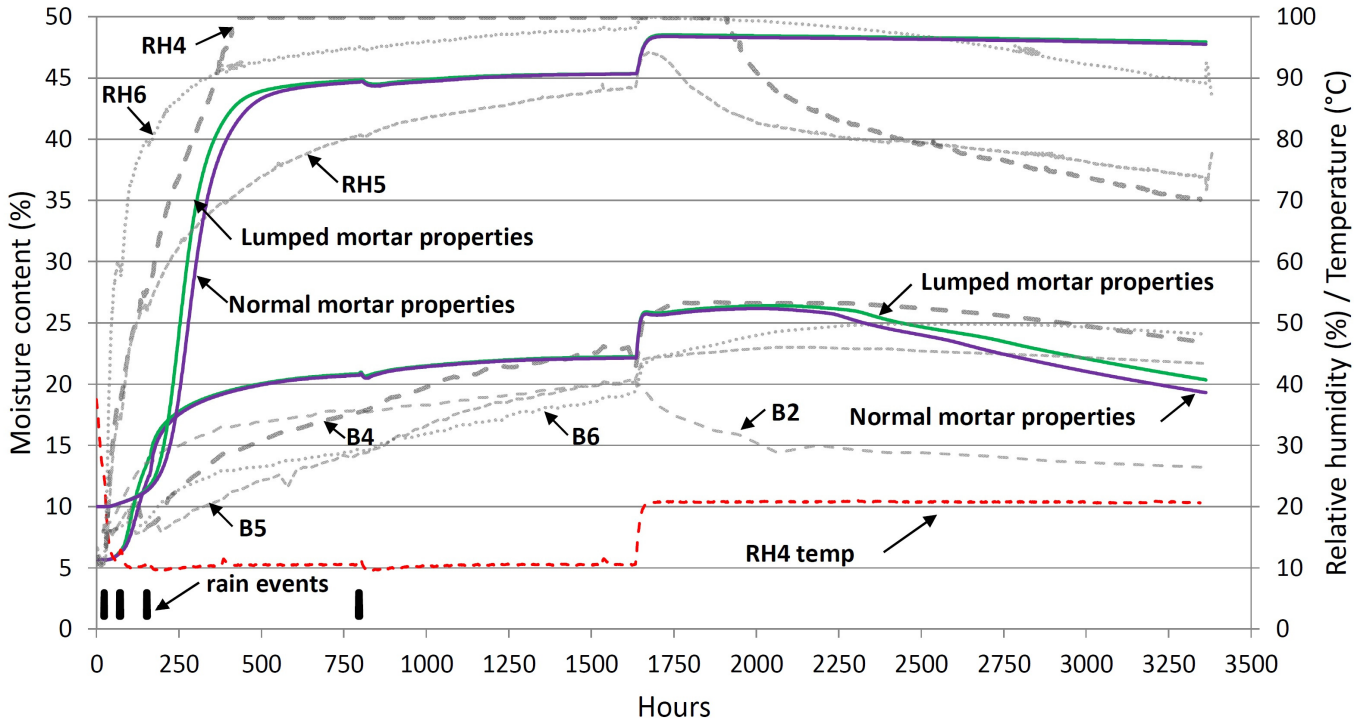

Figure 11. Difference between normal and lumped mortar properties.

4.6. Effect of "Leaky" Joint Inclusion

In the laboratory experiment, recorded video monitoring of segment 2 revealed rapid localized moisture permeation. Figure 12 shows moments from this monitoring, with the visually confirmed extent of the wetted surface area (area of dampness) outlined after the first and second 40 min rain events.

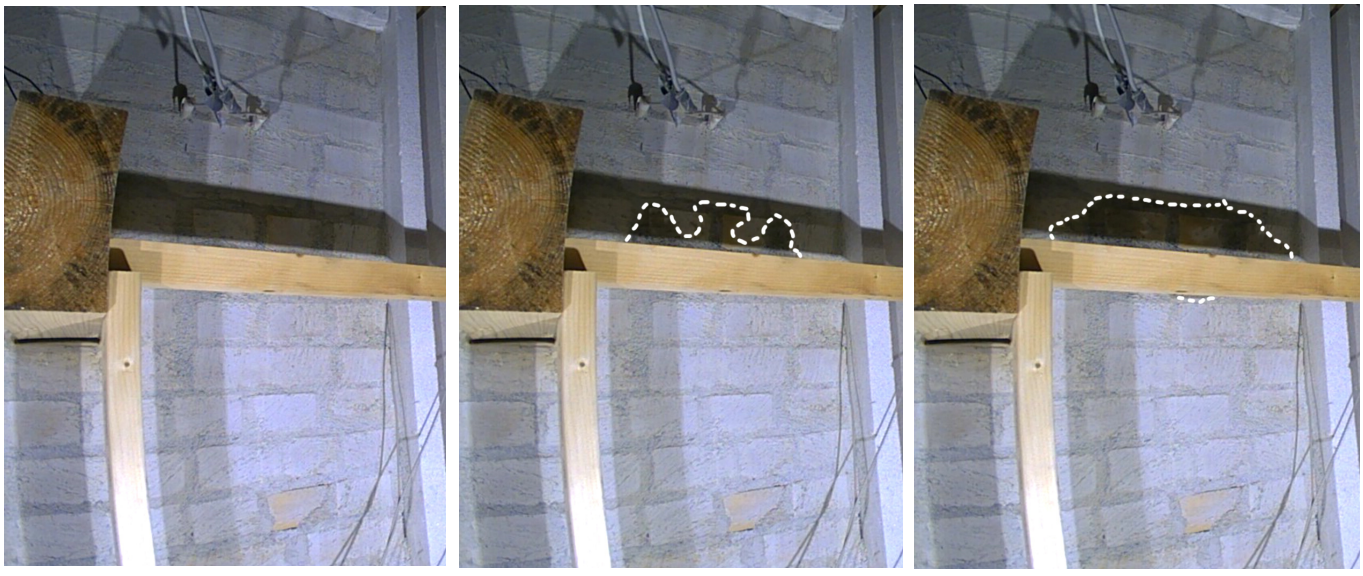

(**a**) (**b**) (**c**)

Figure 12. Segment 2 rain permeation of a mortar joint; (**a**) before rain events, (**b**) after the first 40 min rain event (initiated at 150.6 h), and (**c**) after the second 40 min rain event (initiated at 153.6 h). The extent of the wet masonry surface is outlined.

During the first 40 min rain event (at 150.6 h), the first sign of moisture permeation became visible after only 3 min. This was a very rapid permeation and would indicate a

leak infiltration or interpenetration along a brick–mortar interface, capable of wetting the interior masonry surface.

Due to this observation, a "leaky" mortar joint was modeled with a 10-times higher capillary absorption coefficient (Aw-value), i.e., A_W = 2.5 kg/($m^2s^{1/2}$). That is, it became an extreme case of the lumped properties approach, as a simple, less mesh-intensive alternative to fracture modeling as in [28]. No effort was undertaken to calibrate this Aw-value to measurements, so it should be understood as an example value. Three simulations were then run with one "leaky" mortar joint, respectively, replacing the closest mortar joint below the interior RH sensor and the joint one brick course and two brick courses further below. The results are provided in Figure 13. Including a "leaky" mortar joint just below the sensor provided RH results that showed much faster response time, early on close to RH6. With a "leaky" joint one brick course below, the sensor response was a bit earlier than RH4. "Leaky" joint two brick courses below the sensor also showed early response but with less rapid rise than for the one brick course below.

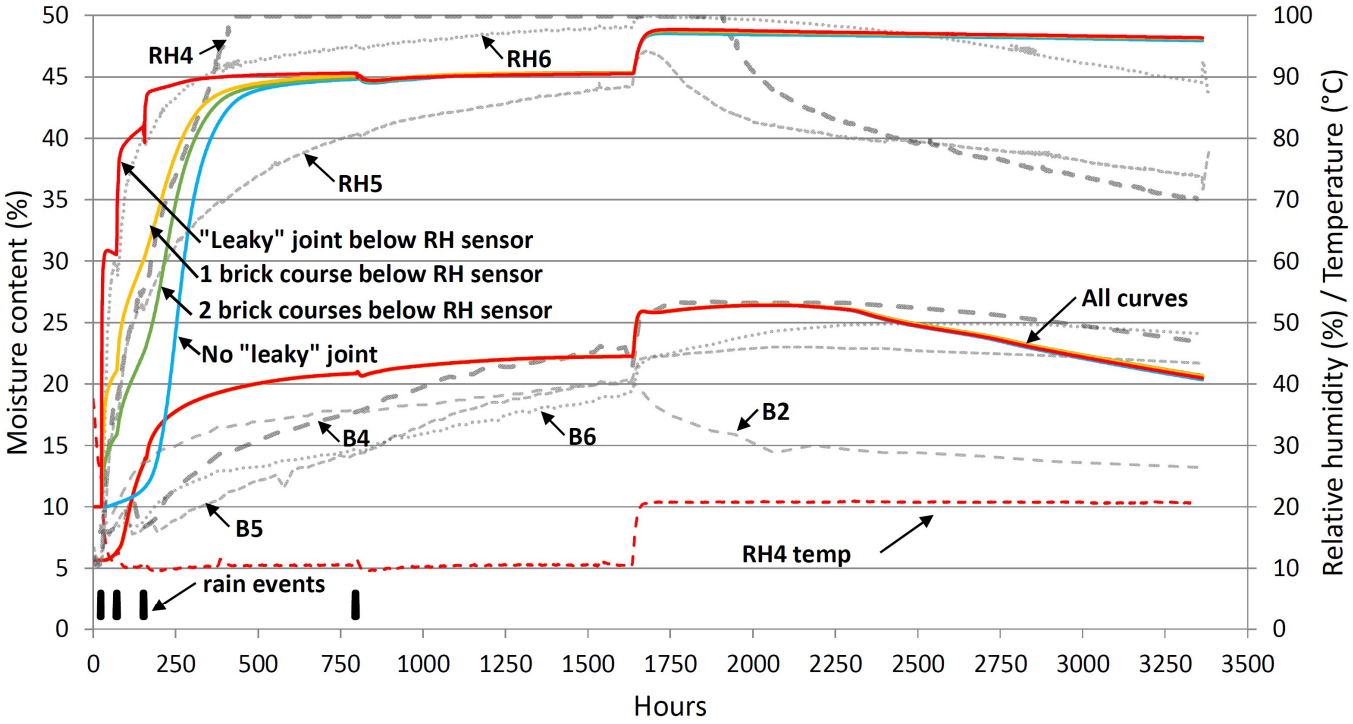

Figure 13. Inclusion of a "leaky" joint just below the sensor, and one brick and two brick courses further below, respectively.

Often the first onset of moisture permeation is observed through the head joint [24]; however, the head joints are not realistically present in a 2D model of the vertical cross-section. Hence, to see the effect of a "leaky" head joint, a 2D model of the horizontal cross-section or, more realistically, a 3D simulation, would be necessary. Permeation through head joints is also observable in Figure 12.

Overall, a "leaky" joint is a 3D occurrence since it would likely have limited extent, whereas in 2D it implicitly has unlimited extent in the missing dimension. 2D results should, therefore, be approached with some care.

4.7. 3D vs. 2D Model

Simulating 3D details like the beam end with a 2D model also introduce uncertainties. Nevertheless, not many studies have provided 3D simulation including beam end. A reason for this is the high numerical complexity and computational requirements associated with a 3D model. Thus, 3D models are usually simplified to homogeneous masonry or layers of masonry and are not of bare brick masonry exposed to rain, see [47,48].

A 3D model was built to investigate the difference compared to the 2D model. The model extents are illustrated in Figure 14a. To limit computational demand, the model takes advantage of axis-symmetry along the center of the beam. Furthermore, the extent of the model is limited around the beam at a distance that from the 2D simulation was indicated to have low impact from the heat and moisture transport occurring around the beam. Due to the limited extent of the 3D model, the RH reading position has been moved two brick courses closer to the beam end. An air layer of 13 mm thickness is present on the side of the beam end, separating it from the masonry.

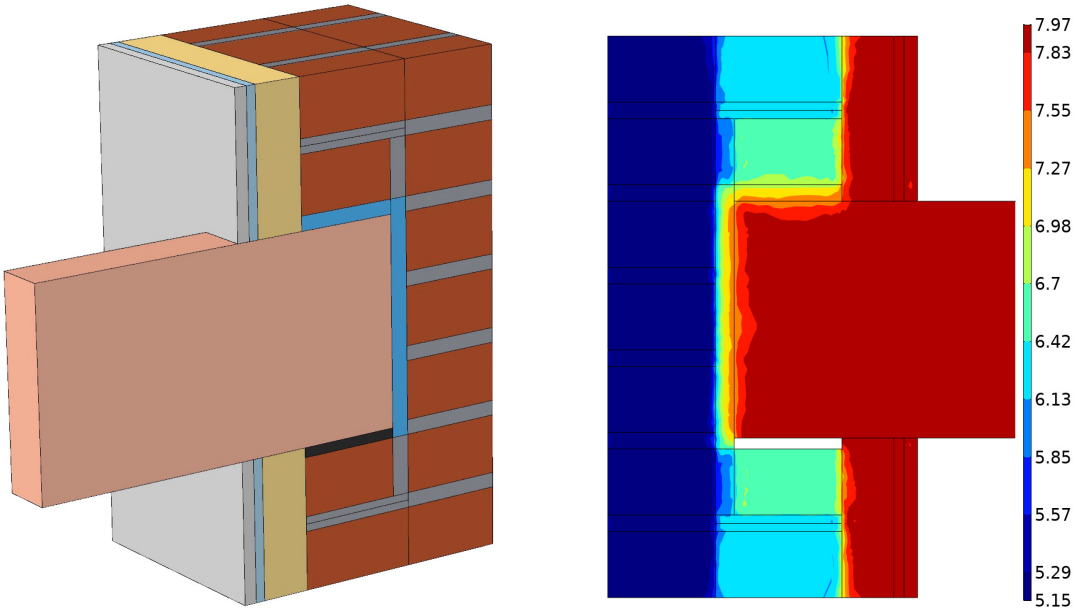

Figure 14. (**a**) Extents of 3D model, and (**b**) initial moisture content distribution given as $\log(p_c)$ at 825 h. The contour plot it generated after gradients are created, thus, sharp initial jumps are smoothed out.

Stable numerical solving of the rain events was not achieved in the 3D model. To avoid simulating the rain events, moisture content after the final rain event, seen from the default 2D simulation, was provided as initial moisture content, with a simplified distribution over the masonry, for a 2D and 3D model setup starting after the final rain event. Figure 14b shows the capillary pressure distribution, applied as initial conditions to distribute the moisture content. The initial temperature was set to 23 °C for the whole structure. Due to time constraints on simulation runtime, another simplification of the 3D model involved having a lower resolution mesh than the 2D model. Somewhat lower accuracy should, therefore, be expected in 3D compared to 2D.

The results of the 2D and 3D simulations using initial moisture contents instead of rain events are given in Figure 15. A difference is seen in the RH results where the 3D simulation shows a higher curve in the cold period. This is, mostly, due to the 3D simulation predicting slightly lower temperature, see Figure 16. However, it can also have been influenced by the moisture distribution (initial or otherwise) acting differently. Furthermore, having moved the reading position closer to the beam end may be the reason for the RH curve becoming slightly lower at the end of the warm period. The default 2D simulation and the 2D simulation with initial moisture provides almost identical results. Also, for the beam end, only slight difference is seen between the two 2D simulations, whereas the 3D simulation provides large deviation to the 2D simulation at the beam end. More moisture is taken up during the cold period and a high level with slow and long dry-out is seen in the warm period. A slightly lower temperature at the beam end is seen in the 3D simulation during the cold period compared to the 2D simulation. These differences are likely due to the beam end in the 3D simulation being surrounded by moist masonry, although separated

by air layers, whereas the 2D simulation implies that the beam end stretches out indefinitely in the missing dimension.

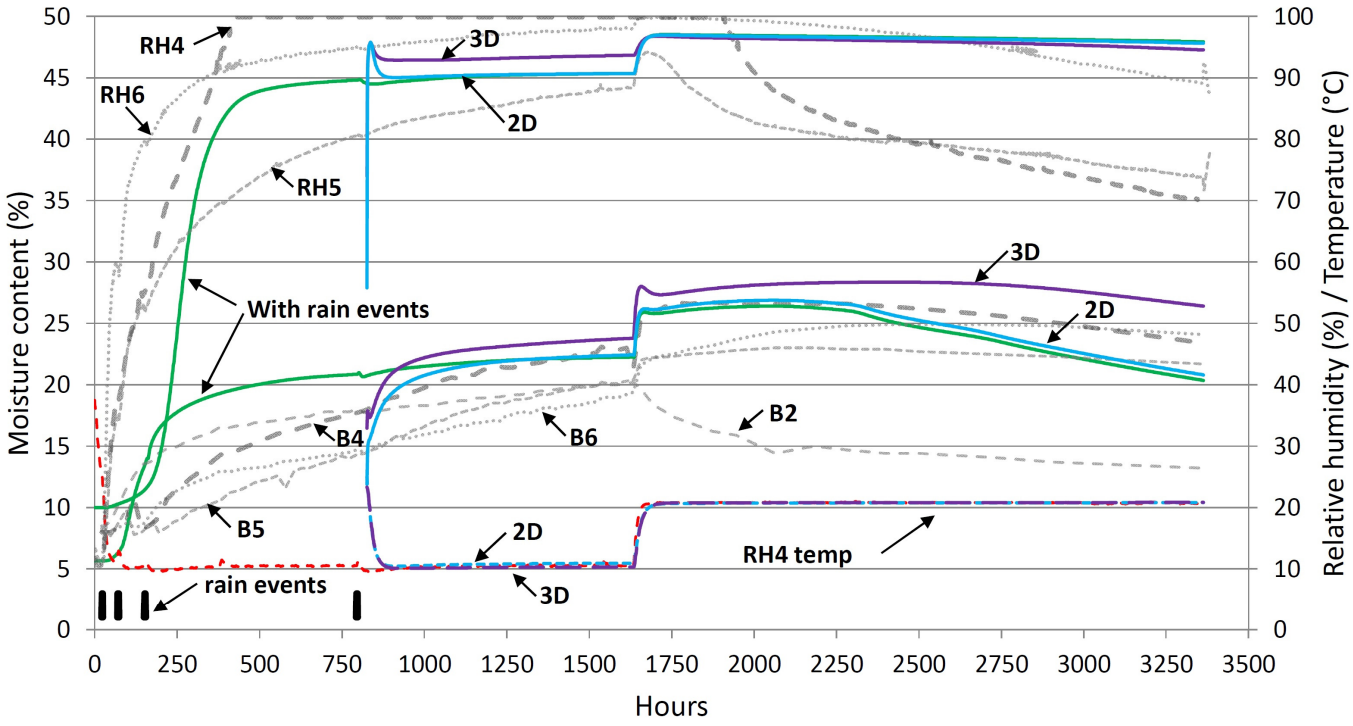

Figure 15. Comparison of 2D to 3D simulation.

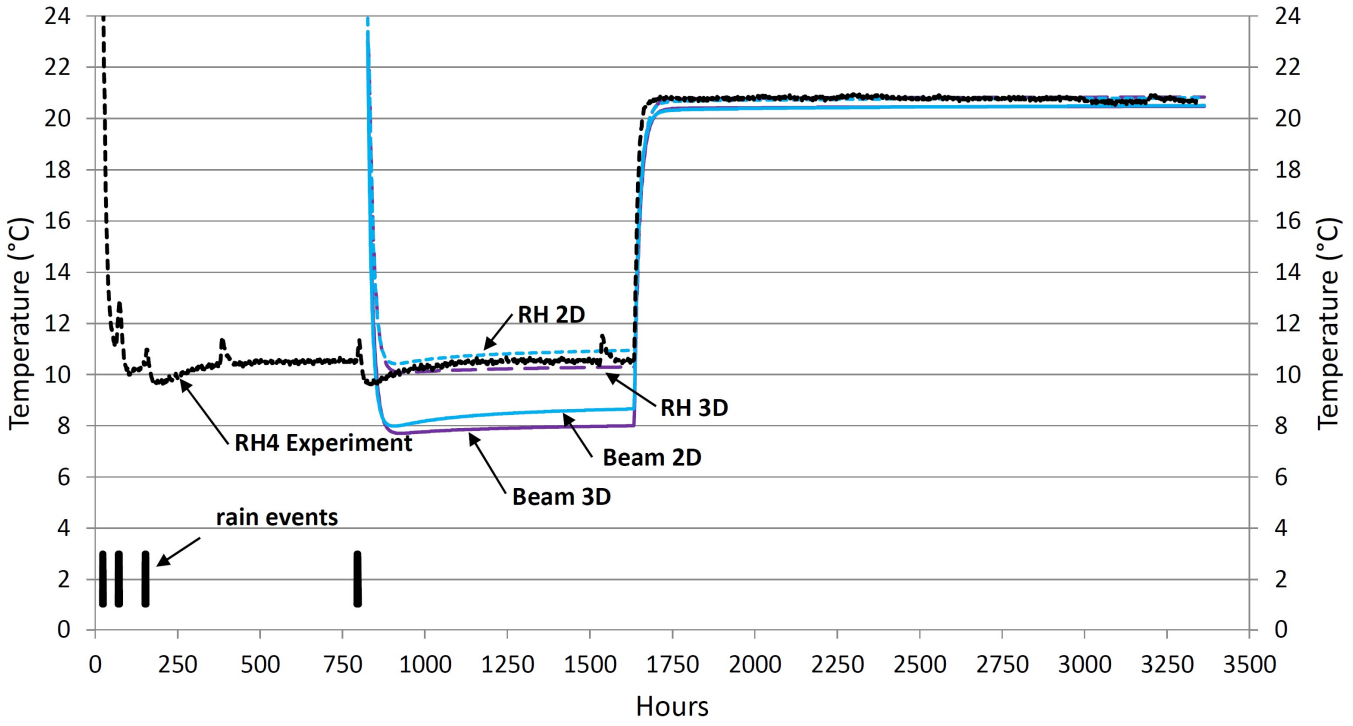

Figure 16. Comparison of 2D and 3D temperature predictions.

4.8. Effect of SVB

Before addressing the effect of SVB, read-out values of the SVB operating status are briefly summarized. During the cold period, the vapor resistance of the SVB decreases simultaneously as moisture from rain events intrudes into the wall. For the unaltered SVB

setup, see Appendix B, the lowest it reached was about $s_d \approx 15.6$ m in the cold period (read in the SVB across the insulation from the RH sensor). In the warm period, the s_d-value slowly increased in the interval $s_d \approx 0.55$–0.57 m with the exception of the scenario with a "leaky" joint next to the sensor which experienced $s_d \approx 0.53$–0.55 m.

Uncertainty accompanies the SVB modeling due to a low resolution in the RH-dependent vapor-resistance test results provided by the SVB documentation. As described in Appendix B, the vapor-resistance values between known values are manually curve-fitted. Consequently, the values are inherently uncertain and might miss the reality.

To investigate effects of the SVB, compared to effects of no-vapor-barrier and traditional polyethylene barrier, simulations were set up with the presumed vapor resistance multiplied by a factor. That factor was given values: 100, 1, 0.5, 0.25, 0.1, and 0.01, where 1 represents the presumed behavior, 100 becomes more like a traditional polyethylene vapor barrier, and 0.01 is close to no vapor barrier. 0.5, 0.25, and 0.1 are added to show intermediate values and the response of the simulation results. Although there are limits to improvement of SVB products, i.e., product development capable of reducing vapor resistance during high RH conditions, intermediate values, at least, provide a notion of improvement potential.

As seen in Figure 17, only minimal RH difference exists between $100s_d$ and $0.10s_d$ up to the onset of warm exterior climate at 1632 h. For the case with very low resistance, i.e., $0.01s_d$, a much quicker rise in RH and a higher RH level are observed. For the drying period after 1632 h, vapor resistance of the SVB has large impact. Although the presumed performance of the applied SVB ($1.0s_d$) does not show much drying, it is, nevertheless, an improvement compared to how a traditional polyethylene vapor barrier would perform ($100s_d$). Lower s_d shows greater drying, with practically no vapor barrier ($0.01s_d$) having the fastest dry-out.

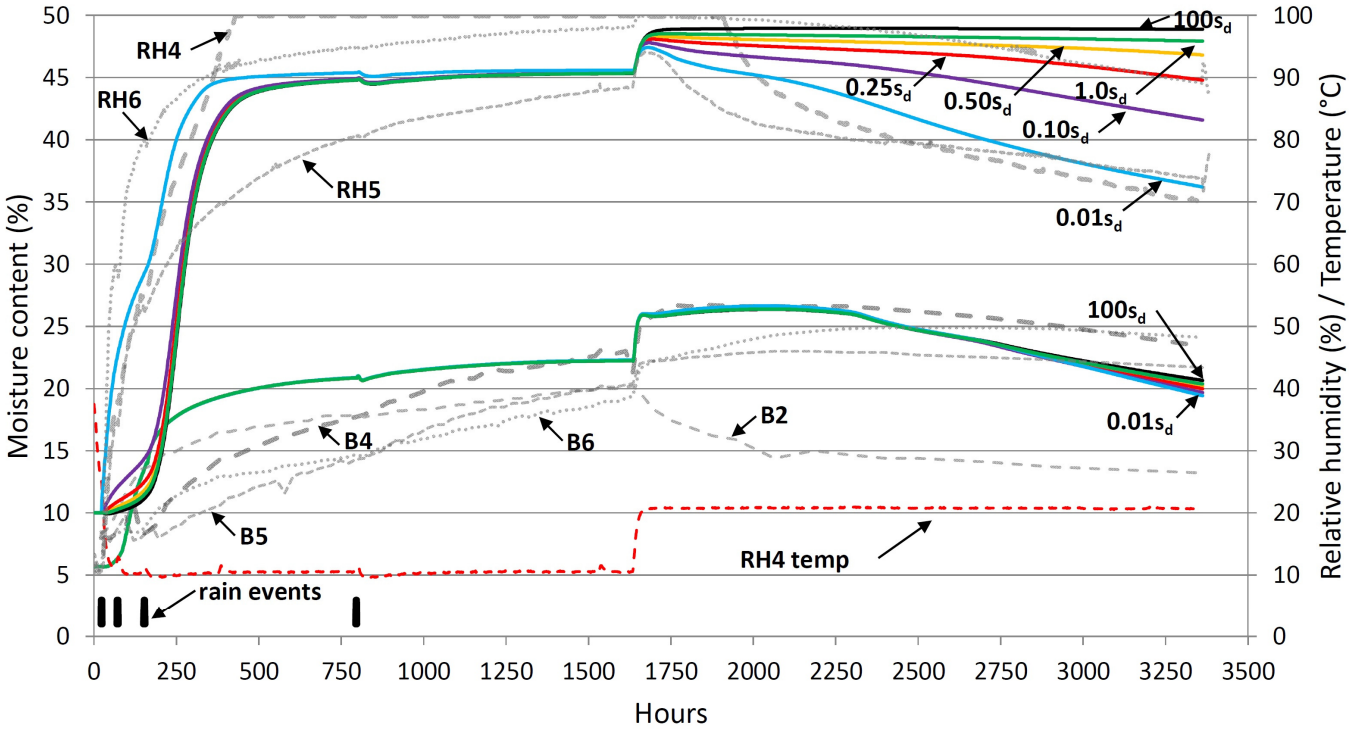

Figure 17. Effect of SVB vapor resistance; multiples of provided/presumed s_d-values, i.e., $1.0s_d$ = values in Appendix B.

In the current simulations, varying the SVB vapor resistance shows a relatively insignificant effect on beam-end drying. It supports the observation in [30] that the beam end shows no clear effect or only minor effect changing from polyethylene vapor barrier to SVB.

5. Discussion

5.1. Numerical Model Issues

Applying sudden rain flux of the magnitude of rapidly wetting the masonry to capillary saturation was found to be leading to some numerical instability. Primarily, the rain is modeled as a step function. Even though the step is given continuous second-derivative smoothing over 60 s, the numerical simulation struggles with the abruptness and magnitude of the rain load, especially when the exterior surface is relatively dry prior to the rain. Several aspects were found to have an impact on this situation.

During establishment of the model, it was discovered that the numerical stability was impacted by the retention curve, with sharp jumps giving more numerical instability than smooth retention curves. Similarly, Gutland et al. [28] reported numerical issues if the retention curve was to be modeled as a step function (the most extreme case of sharp retention curve), in the hygrothermal simulation software DELPHIN.

Janssen et al. [49] addressed oscillations observed at the toe of the moisture front, where oscillation magnitude was found to be dependent on initial moisture content and mesh discretization. They concluded that such oscillation had a limited effect on the overall result over time. Furthermore, they argued that with natural climate exposure one will rarely experience such sharp moisture fronts, making such simulations even less affected by this issue. The findings of Janssen et al. are similar to observations during the current study, although the issue has not been explicitly studied. However, oscillations localized somewhere along the moisture front toe (2D), sometimes severe, are observed. Nevertheless, the simulation quickly becomes corrected, erasing the trace of the oscillation in a relatively short time span (a few hours), compared to the overall duration of the simulation case. Still, numerical instability may be caused by such oscillation, leading to situations where the numerical iteration does not converge well.

COMSOL will, in situations where the iterative numerical solution does not converge and satisfy the tolerance criteria, try smaller and smaller timesteps. With repeated no convergence, the timesteps become untenably small.

It was found that, in some cases, a couple of measures could improve numerical solving (prevent or rein in small timesteps). The model can be relaxed with regard to the rain load when numerical convergence becomes poor (small timesteps) during absorption from rain events. This involves the rain load being relaxed linearly when at times the convergence timesteps become small, e.g., <0.02 s, so that 0.002 s timesteps only have a 1/10 of the rain load. Similarly, the masonry absorption-capacity can be relaxed linearly for timesteps, e.g., <0.1 s. These two relaxations do not occur simultaneously, with the second only applying when the exterior surface moisture content becomes close to saturation. Additionally, the rain flux can be modeled as linearly diminishing over a capillary pressure range, e.g., 1351 Pa > p_c > 13.5 Pa (0.99999 < ϕ < 0.9999999 at 20 °C), which is well below the overall moisture retention interval of capillary pressure for brick and mortar. These two measures with the aforementioned values were implemented in the simulations of the present study.

The numerical instability is believed to be caused by either or both the sharp moisture front gradient, creating oscillation with under- and overshooting at the moisture front toe, and the possible overshooting of the saturated moisture content from one timestep to the next, creating difficulties with numerical handling. This is also influenced by interaction between brick and mortar when they have very different capillary conductivities.

5.2. Capillary Model Evaluation

To assess the rain absorption of the model, a simple one-brick geometry was simulated with exposure to the rain for two hours through the brick face. From the simulation with the default hydraulic-conductivity curve a result of A_w = 0.194 kg/(m^{2}s$^{1/2}$) was calculated. This value is considered reasonably close to the measured absorption coefficient A_w = 0.188 kg/(m^{2}s$^{1/2}$), which was used as input to generate the capillary-conductivity curve applied in the model. For comparison, the max-setup (Section 4.2) pro-

vided A_w = 0.182 kg/($m^2s^{1/2}$) and the min-setup gave A_w = 0.174 kg/($m^2s^{1/2}$). Whereas the min-setup is deemed to behave logically, the max-setup gave surprisingly low value and seemed to attract some more numerical instability, possibly causing it to underestimate the absorption rate. Overall, the values indicated that the model approaches rain absorption as severely as free liquid absorption in an absorption experiment. Similarly, normal and lumped mortar properties, respectively, resulted in A_w = 0.023 kg/($m^2s^{1/2}$) and A_w = 0.22 kg/($m^2s^{1/2}$), fairly close to the 0.025 and 0.25 kg/($m^2s^{1/2}$), respectively, applied as input to generate the capillary conductivity.

Although the simulated A_w-values came close to the measured/intended values, the correctness of the hydraulic-conductivity curves is not thereby implied. For instance, Janssen [50] showed the same capillary-absorption results could be produced from different conductivity curves, including having variation in the conductivity at capillary saturation. To further evaluate accuracy, laboratory measurements of moisture front profiles would be needed for comparison to profiles from simulations. Such profiles are furthermore influenced by the retention curve which is unknown for the specific brick.

5.3. Material Properties and Model Uncertainties

The simulations show some significant deviations to the experiment results. Especially the RH sensors RH4 and RH5 show a drying trend that has not been replicated, nor attempted to be replicated, within the current study and model framework. This is partly due to the conservative approach of the simulation study, which likely overestimates the moisture uptake of the masonry. Nevertheless, uncertainty with both material properties and conservative boundary conditions impacts overestimation of moisture content. To elaborate on this, possible explanations for the observed deviations can be:

- There might be less overall rain uptake in the masonry, due to runoff, in combination with "leaky" joint interfaces enabling leak-like intrusions (infiltrations) through the masonry. This would enable the RH sensor to still show rapid response to rain, while the masonry overall would store less moisture needing to be dried out inwards through the SVB; this, plausibly in combination with interface resistances, lower acting capillary conductivities, or higher vapor diffusivities for the rest of the masonry;
- The exterior finish of the masonry having been brushed with heavily wetted mortar [30] could have closed the surface pores of the bricks, or created a surface coating, that reduces moisture absorption of the bricks;
- The interior insulation structure and mounting of the SVB in the experiment may have been less air-tight than presumed in the simulation model.

Furthermore, the drying rate of the beam end at the end of the warm period is larger in the 2D simulation than indicated in the experiment. As seen in Section 4.7, a 3D simulation shows a much more severe situation for the beam end. This result differs from the findings of [47,48], which indicated that 2D simulations were able to replicate measured results very well, with only small differences seen between 2D and 3D simulations. A reason for why these results differ is likely due to the differences in scenario, with the present study covering severe rain wetting of bare brick masonry, whereas the other studies involve lower rain severity in combination with external render and thicker masonry, including applying layered masonry models instead of modeling all mortar joints.

Regarding the SVB modeling, there is also some uncertainty. Unknown intermediate vapor resistance values for the SVB and possible, but unknown, directional dependence, rendered the modeling difficult and uncertain (see Appendix B). It is plausible that the SVB has a lower vapor resistance than what was modeled in certain RH ranges. To include SVB functionality more confidently in hygrothermal simulation models, there is a need for documentation of SVBs that provides more information and considerably higher resolution in s_d-values over the RH-range than what were available.

5.4. Conservative Modeling Philosophy

When conducting hygrothermal simulations for comparison to experiment results, one can question the intended purpose. That is, should the simulation aim at replicating specific results with low error of deviation or should it provide a conservative result that with a safety margin envelopes experiment results? This becomes an important question when acknowledging that the experiment results show a large span in behavior; in fact, behaviors differing so much that one could believe they were stemming from differently constructed masonry walls. However, it mainly confirms the diversity or heterogeneity of masonry regarding moisture transport, especially relevant for bare external masonry façades exposed to driving rain. Replicating specific results from experiments might, therefore, be unrealistic. This corresponds with; that heat, air, and moisture transport models (HAM models) have been attributed with providing good results in problems where the aim is to reproduce patterns [51].

Whether insurance of conservative results should be sought is not often addressed or pondered (we here exclude such discussions in topics on numerical methods and numerical solving). The "question of conservative" is more commonly discussed regarding selection of a moisture reference year or the use of damage indexes, e.g., mold or frost risk models. For instance, the European standard EN 15026 [52] states that a moisture reference year should reflect the most severe conditions likely to occur every 10 years. A 10-year return period has been deemed appropriate, intending that it allows moisture accumulated in "a bad year" to dry out in subsequent years [53]. Regarding mold models, Johansson et al. [54] suggests predictions should have a safety margin, i.e., the models should be conservative; although, the safety margin should not be excessive, due to the extra costs that would entail. With humidity loads often being the cause of building envelope deterioration and limited service-life, Kalamees [55] states that the common practice of neglecting safety factors in hygrothermal design deserves some criticism. Hens [56] harshly criticizes the practice of hygrothermal modeling as modeling fiction. That is, geometry, material properties, climate exposure, contact conditions, and initial conditions are not well known; nevertheless, they are modeled as well defined in deterministic models. Models should address probability and risk, not only be able to model very specific cases of extremely simplistic building parts [56]. An emerging discipline of probabilistic hygrothermal simulation-based risk assessment [36,57,58] has, to some extent, met this call for interior insulated masonry by combining hygrothermal simulation with Monte Carlo simulation. These studies assess the probabilistic sensitivity occurring from input values (e.g., properties and boundary condition coefficients) described with probability distributions. However, hygrothermal-simulation modeling choices or approaches, within the framework of probabilistic risk assessment of degrees of model reliability, are not particularly addressed. That is, less discussed is how to ensure conservative model design, or model design which does not fail to reveal conflict with the initiation or serviceability limit state. The initiation limit state is defined by ISO 13823 as "*state that corresponds to the initiation of significant deterioration of a component of the structure*" [59]. Implementation of serviceability limit state (SLS) analysis following ISO 13823 is discussed by Lacasse and Morelli [60]; herein, with focus on climate-exposure input and hygrothermal-simulation results for use in damage indexes (RHT index) in a comparative capacity. One modeling aspect is addressed by including different degrees of moisture deposition on a sill plate in a stucco-clad wood-frame wall to illustrate impact on the RHT index. Nevertheless, the modeling aspect is not particularly discussed in relation to the SLS analysis. They conclude the hygrothermal SLS approach has merit, albeit not yet fully explored [60]. As another example, rain infiltration in brick-veneer walls has, to some extent, been investigated and discussed in terms of modeling choices [13,24,61,62]. Similar insight is, however, limited in regard to historic masonry [61]. However, two studies should be mentioned. Simplifications of modeling masonry as a homogenous brick layer (1D) instead of a brick–mortar composite (2D), with and without interface resistances, were investigated by Vereecken and Roels [21]. Their study insightfully demonstrated the parts both brick and mortar played in moisture transport and

distribution. Moisture transport along brick–mortar interfaces were not included. That, however, was addressed by Gutland et al. [28] who provided a modeling methodology for increased moisture transport along the brick–mortar interface and demonstrated its functionality and performance. However, these studies were rather limited in geometric extent, focusing on interaction between a few bricks and joints, and did not address performance of interior insulation retrofit in this regard. Thus, more insight is needed into whether models represent correct transfer mechanisms. The term transfer mechanisms is taken from ISO 13823 [59,63].

While the current study does not address probability distributions and probabilistic sensitivity from material properties, contact conditions, or initial conditions, the simulations have been established with an attempted conservative approach of rainwater absorption. This has been apporached by ensuring the maximum amount of rainwater absorption that material properties of brick and mortar allow for, including accounting for increased absorption of the brick–mortar interface. Nevertheless, this was not sufficient to recreate the rapid RH-response (all sensors) and the high RH levels (RH4) on the inside of the masonry during the cold period seen in the experiments. Including a "leaky" joint to resemble an infiltration leak was necessary to approach conservative RH-response results, whereas a 3D model was found necessary to provide slow dry-out of beam ends and conservative results during the warm period. Scrutiny regarding results reading position compared to sensor extents has also been shown to be useful. This should be a call for a discussion regarding how such, or similar, masonry structures should be modeled to uphold confidence of result conservativeness.

6. Conclusions

The study applies a conservative 2D simulation model to investigate and demonstrate the impact of uncertainty and modeling choices, with the simulation results compared to results of an experiment for a check of realism. The simulation model is very conservative in the aspect of allowing high rain absorption and, consequently, high moisture content in the wall. This approach is seen to underestimate the water transport of "leaky" joints. Including "leaky" joints with substantially higher moisture transport in the model is shown to produce RH response in line with the more severe laboratory results at the masonry interior surface. At the same time, the 2D model underestimates the long drying out times of the beam end. When applying a 3D model for comparison, a substantially higher moisture content and longer dry-out time is predicted for the beam end. Nevertheless, the conservative approach likely becomes too severe, failing to replicate the distinct drying trend seen in two of the RH-sensor data on the masonry interior surface. It is believed several factors, such as rain-absorption effectiveness, capillary conductivities and interface resistances in the masonry, SVB vapor resistance, and non-homogeneous material properties, affect the situation simultaneously, making the experiment drying trend less severe than the results of the basis simulation. This highlights a question of how to model correct moisture-transfer mechanism to uphold model confidence. This, especially, applies to bare brick masonry exposed to severe rain, where the rain absorption may follow infiltration pathways.

The conclusion is summarized as follows:

- Uncertainty in hydraulic conductivity curves for brick and mortar are clearly impacting results, with a large impact on response of RH sensors to rain events, and on the dry-out of beam ends. Large uncertainty regarding the mortar capillary absorption coefficient was likely the dominant cause;
- Altering the retention curves, including subsequent impact on hydraulic-conductivity curves, had moderate to minor impact on the results. However, with the model operating around the highest RH range that the RH readings could detect at the reading location, and with some uncertainty regarding numerical solving, the true impact of altering the retention curves became obscured;

- RH results are sensitive to the results reading position in the model when comparing simulation to experiment, for the experiment sensor located interior to the masonry surface at the masonry–insulation interface. Similar is the case for the beam-end moisture sensor, regarding at what depth into the modeled wood readings are conducted. Consideration should be given to sensor location and behavior in experiments when choosing reading position and when evaluating simulation results;
- Modeling wooden beam end as anisotropic instead of isotropic does influence simulation results;
- Lumping moisture transport along the brick–mortar interface with mortar properties does show more rapid RH response and slightly increased RH at interior masonry surface. It, furthermore, increases moisture content at the beam end compared to results with normal mortar properties. However, the effect is not large enough to ensure the rapid RH response seen of RH sensors to rain events;
- Inclusion of a "leaky" mortar joint, representing considerably faster moisture permeation from rain events along the brick–mortar interface provides results more in line with the rapid RH-sensor response seen in experiment. The inclusion of a "leaky" mortar joint is supported by experiment observations;
- Conservative beam-end moisture content is neither achieved with normal mortar properties nor with lumped properties in 2D simulation. In contrast, a 3D simulation is seen to give much higher moisture content in the beam end and longer dry-out times providing highly conservative results;
- Vapor resistance of SVB has low influence on results during the cold exterior climate. With warm climate, the dry-out towards the interior are highly dependent on SVB vapor resistance. If further product development could achieve lower vapor resistance of a SVB product for high RH environments, this could provide significant benefits with regard to dry-out performance;
- Vapor resistance of SVB has almost insignificant influence on beam-end dry-out under the studied conditions;
- The (conservative) modeling approach clearly overestimated moisture content in the masonry, and within the conservative model framework the distinct dry-out trend seen in two of the three experiment wall segments investigated was not replicated, the model, thus, giving indication of being too conservative in some respects.

Author Contributions: Conceptualization, J.I.K.; methodology, J.I.K.; software, J.I.K.; validation, J.I.K.; formal analysis, J.I.K.; investigation, J.I.K.; data curation, J.I.K.; writing—original draft preparation, J.I.K.; writing—review and editing, J.I.K., T.K. and S.G.; visualization, J.I.K.; supervision, T.K. and S.G. All authors have read and agreed to the published version of the manuscript.

Funding: The authors gratefully acknowledge the financial support by the Research Council of Norway and several partners through the Centre for Research-based Innovation "Klima 2050" (grant no. 237859) (www.klima2050.no).

Data Availability Statement: Data sharing is not applicable to this article.

Acknowledgments: Lab engineer Ole Aunrønning is acknowledged for an invaluable contribution with wall and equipment assembly, material property testing, and measurement monitoring.

Conflicts of Interest: The authors declare no conflict of interest.

Appendix A Hygrothermal Formulas and Material Properties

The retention curve is given by Equation (A1) which is a multimodal version of an expression proposed by Carmeliet and Roels [64]. For more details, see [17].

$$w = w_{\lim} \underbrace{\left[\exp\left(-\frac{P_c}{\rho_w R_w T}\right)\right]}_{=\phi}^{n_{w,0}} + (w_{cap} - w_{\lim}) \sum_{i=1}^{N=4} \left(l_{w,i} \left[1 + (c_{w,i} P_c)^{n_{w,i}}\right]^{\left(\frac{1-n_{w,i}}{n_{w,i}}\right)} \right) \quad \text{(A1)}$$

where $w_{\lim}$ would be the limiting, critical water content between the hygroscopic and over-hygroscopic region; however, the actual $w_{\lim}$-value could be expected to deviate from the critical moisture content, being a more arbitrary fitting parameter [64]. w_{cap} moisture content at capillary saturation, P_c capillary pressure, ρ_w density of water, R_w specific gas constant for water vapor, $n_{w,0}$ fitting exponent, $l_{w,i}$ weighing coefficient equal to the share of pores associated with the corresponding inflection point in cumulative pore-size distribution, i.e., $\Sigma l_{w,i} = 1$, $c_{w,i}$ inverse of P_c at inflection point, and $n_{w,i}$ fitting exponent. Material properties are provided in Table A1 and coefficients in Table A2.

The vapor diffusivity is taken as Equation (A2) which is a combination of Schirmer's equation [65] and the scaling expression of the serial–parallel pore model [66] accounting for liquid moisture content. The vapor-resistance coefficient μ_{dry} correlates the permeability to a porous material, with μ_{dry} determined by dry cup measurements.

$$\delta_v = \frac{1}{R_w T} \frac{2.306 \cdot 10^{-5}}{\mu_{dry}} \left(\frac{P_0}{P_a}\right) \left(\frac{T}{T_0}\right)^{1.81} \frac{\left(1 - \frac{w}{w_{sat}}\right)}{p + \left(1 - \frac{w}{w_{sat}}\right)^2 (1 - p)} \quad \text{(A2)}$$

with P_0 and P_a, respectively, the standard and acting atmospheric pressure, $T_0 = 273.15$ K, p is the volumetric fraction that is parallel pore domain [18], p has simply been set to $p = 0.497$ [8,44] for all materials, although p is material-dependent [66], and using a constant for p has been disputed [18].

The moisture-dependent thermal conductivity is expressed as Equation (A3). A second-order correction for moisture content is included to better represent insulation materials. Use of Equation (A3) is a necessary simplification due to lack of conductivity measurements. In reality, a highly non-linear relationship to moisture content may exist, which is better represented with, for instance, the formulas in [67]. Coefficients and background for Equation (A3) are listed in Table A3.

$$\lambda_{eff} = \lambda + b_{w1} \frac{w}{w_{sat}} + b_{w2} \left(\frac{w}{w_{sat}}\right)^2 \quad \text{(A3)}$$

where λ [W/(m·K)] is dry thermal conductivity, and b_{w1} and b_{w2} [W/(m·K)] correction coefficients for moisture content.

From testing in our laboratory, we have found A_w-values for mortar joints when including absorption effect from the brick–mortar interfaces parallel to absorption direction to be in the range 0.14–0.44 kg/(m^{2}s$^{1/2}$). Although these values have a wide span, they can be said to be closer to the brick A_w-value of 0.188 kg/(m^{2}s$^{1/2}$) than the mortar A_w-value (0.01–0.04 kg/(m^{2}s$^{1/2}$) [30]). The highest value in the span might be unrealistic for the wall that we are simulating since measures were made to achieve a rather good-quality brick–mortar interface, more similar to test samples representing the lower range of the span. However, these samples were constructed with similar, but slightly different, bricks and mortar, thereby, introducing uncertainty. As a guesstimate, we chose to apply an A_w-value of 0.25 kg/(m^{2}s$^{1/2}$), a factor of 10 higher than the normal absorption value, for mortar joints parallel to absorption direction during rain events. Outside of rain events, the intermediate A_w-value of mortar 0.025 kg/(m^{2}s$^{1/2}$) is applied to calculate hydraulic conductivity.

Table A1. Applied material properties.

Material	w_{sat} [kg/m^3]	w_{cap} [kg/m^3]	$w_{\lim}$ [kg/m^3]	A_w [kg/(m^{2}s$^{1/2}$)]	μ_{dry} [-]	λ [W/(m·K)]	c_p [J/(kg·K)]	ρ [kg/m^3]
Brick high IRA	310.8 [a]	255.74 [a]	2.5 [e]	0.188 [a]	13.36 [a]	0.45 [c]	1000 [c]	1723 [a]
LC mortar	294 [a]	258.79 [a]	18 [e]	0.025 [a]	18.81 [a]	0.82 [c]	1000 [c]	1806 [a]
Gypsum	720 [d]	353 [d]	6 [e]	0.0397 [d]	6 [b]	0.25 [b]	850 [d]	720 [b]
Spruce longitudinal	600	600 [d]	60 [e]	0.00688 [d]	4.213 [d]	0.23 [d]	1500	455 [d]
Spruce radial/tangential	600	600 [d]	60 [e]	0.000933 [d]	8.426 [f]	0.09 [d]	1500	455 [d]
Mineral wool	992 [d]	232 [d]	0.61 [e]	-	1.3 [d]	0.034 [b]	850 [d]	17 [b]
Asphalt sill gasket	-	-	-	-	-	0.553	1500	1200

[a] measured, refer [30], w_{sat} a guestimate based on measurements. [b] product declaration. [c] in accordance with EN 1745 [68]. [d] WUFI material database [46]. [e] curve fitting to sorption/retention curves. [f] arbitrary choice taking into account radial and tangential directions, and occurrence of cracks.

Table A2. Coefficients for retention curves, expression (A1).

Material	$n_{w,0}$	$l_{w,1}$	$l_{w,2}$	$l_{w,3}$	$l_{w,4}$	$c_{w,1}$	$c_{w,2}$	$c_{w,3}$	$c_{w,4}$	$n_{w,1}$	$n_{w,2}$	$n_{w,3}$	$n_{w,4}$
Brick high IRA [a]	0.7	0.12	0.66	0.22	0	8.67×10^{-7}	6.72×10^{-6}	4.00×10^{-5}	-	4	4	5	-
LC mortar [b]	0.4	0.07	0.55	0.36	0.02	7.41×10^{-8}	4.20×10^{-7}	1.13×10^{-6}	2.00×10^{-5}	3	5	4	2
Gypsum [c]	1.2	0.11	0.44	0.35	0.10	1.81×10^{-7}	2.24×10^{-6}	5.52×10^{-6}	1.48×10^{-5}	2.6	6	4	1.8
Spruce [c]	0.6	0.10	0.50	0.30	0.10	7.02×10^{-8}	1.03×10^{-6}	3.43×10^{-6}	6.18×10^{-5}	2.2	5	1.8	1.6
Mineral wool [c]	4	0.13	0.51	0.36	0	2.06×10^{-6}	1.48×10^{-5}	7.40×10^{-5}	-	5	2.8	1.8	-

[a] curve fitting to a retention curve trend of a presumed similar brick, accounting for the measured sorption curve. [b] curve fitting to retention curve trend, of a presumed representative mortar, that is, shifted on the capillary pressure axis to fit with the measured sorption curve. [c] curve fitting to retention curves taken from WUFI material database [46].

Table A3. Conductivity correction coefficients.

Material	λ_{sat} [W/(m·K)] [a]	b_{w1} [W/(m·K)]	b_{w2} [W/(m·K)]
Brick high IRA	1.35 [b]	0.9	0
LC mortar	1.5 [b]	0.68	0
Gypsum	1.16 [b]	0.91	0
Spruce	0.7097 [b]	0.4797	0
Mineral wool	0.5975 [c]	0.0159	0.5476
Asphalt sill gasket	0.553	0	0

[a] effective conductivity at saturation. [b] inspired by WUFI material database [46]. [c] conductivity of water at 293.15 K.

Appendix B Modeling of the SVB

The SVB is modeled as a material with a notional thickness of 10 mm. Heat capacity and conductivity are scaled with factor 1/20 and 20, respectively, to account for the ratio of notional thickness to actual thickness. Sorption is set equal to mineral wool without conducting scaling, in lack of better estimates.

Vapor-diffusion resistance is modelled as dependent on RH on each side of the SVB. Table A4 provides a matrix of sd-values found from manual curve fitting to a limited set of measured values (underlined in Table A4) provided by a technical approval document for the SVB. The matrix is rendered symmetric, i.e., assuming s_d-values are independent of SVB orientation, due to lack of information or data specifying otherwise. However, directional dependence of SVBs or smart vapor retarders (SVRs) is common, e.g., [69], and, consequently, to account for directional dependence such a matrix should be non-symmetric. For visual perception, resultant curves are provided in Figure A1. One perceived outlier (s_d = 3 m at 75/25% RH) was excluded since it did not fit with the other data; however, it might be plausible that s_d = 8 m at 75/33% RH could be an outlier instead, or also, which perceivably would radically lower s_d-values in the affected region.

Table A4. SVB s_d-values (m) as function of RH at both sides of the barrier. Bold, underlined numbers are measured values originating from the technical approval document of the SVB, with one outlier (presumed wrong) placed in parenthesis.

RH\RH	**0**	**11**	**25**	**30**	**33**	**40**	**45**	**50**	**55**	**60**	**65**	**70**	**75**	**80**	**85**	**90**	**95**	**100**
0	107	104	**100**	96.8	93	82	73	63	52	42	32	22	**14**	8.6	4.4	1.4	0.43	0.26
11	104	101	97.5	94	90	79.6	70	60	50	40	30	20.5	**12**	7	3.6	1.15	**0.36**	0.22
25	**100**	97.5	92	89	86	76	66.5	57	46	37	28	19	10 (**3**)	5.4	2.6	0.82	0.29	0.174
30	96.8	94	89	86	83	73	63	53	43	34	26	17	9	4.9	1.9	0.7	0.265	0.158
33	93	90	86	83	79	68	58	**48**	38.5	30	22	14.8	**8**	3.9	1.45	0.62	0.25	0.148
40	82	79.6	76	73	68	52	40	30	23	17	11.5	7.5	4.1	2	0.92	0.46	0.22	0.127
45	73	70	66.5	63	58	40	28.5	21	15	10.5	7	4.2	2.4	1.2	0.7	0.37	0.2	0.114
50	63	60	57	53	**48**	30	21	15	10	6.9	4.4	2.65	**1.4**	0.88	0.54	0.3	**0.18**	0.102
55	52	50	46	43	38.5	23	15	10	6.8	4.8	3.1	1.7	0.96	0.65	0.42	0.25	0.16	0.091
60	42	40	37	34	30	17	10.5	6.9	4.8	3.2	2.1	1.21	0.74	0.51	0.32	0.21	0.14	0.08
65	32	30	28	26	22	11.5	7	4.4	3.1	2.1	1.42	0.9	0.58	0.4	0.26	0.18	0.12	0.07
70	22	20.5	19	17	14.8	7.5	4.2	2.65	1.7	1.21	0.9	0.65	0.45	0.31	0.22	0.155	0.105	0.06
75	**14**	**12**	10 (**3**)	9	**8**	4.1	2.4	**1.4**	0.96	0.74	0.58	0.45	0.34	0.24	**0.18**	0.13	0.09	0.052
80	8.6	7	5.4	4.9	3.9	2	1.2	0.88	0.65	0.51	0.4	0.31	0.24	0.19	0.145	0.105	0.075	0.045
85	4.4	3.6	2.6	1.9	1.45	0.92	0.7	0.54	0.42	0.32	0.26	0.22	0.18	0.145	0.115	0.085	0.06	0.04
90	1.4	1.15	0.82	0.7	0.62	0.46	0.37	0.3	0.25	0.21	0.18	0.155	0.13	0.105	0.085	0.065	0.05	0.035
95	0.43	**0.36**	0.29	0.265	0.25	0.22	0.2	**0.18**	0.16	0.14	0.12	0.105	0.09	0.075	0.06	0.05	0.04	**0.03**
100	0.26	0.22	0.174	0.158	0.148	0.127	0.114	0.102	0.091	0.08	0.07	0.06	0.052	0.045	0.04	0.035	**0.03**	0.025

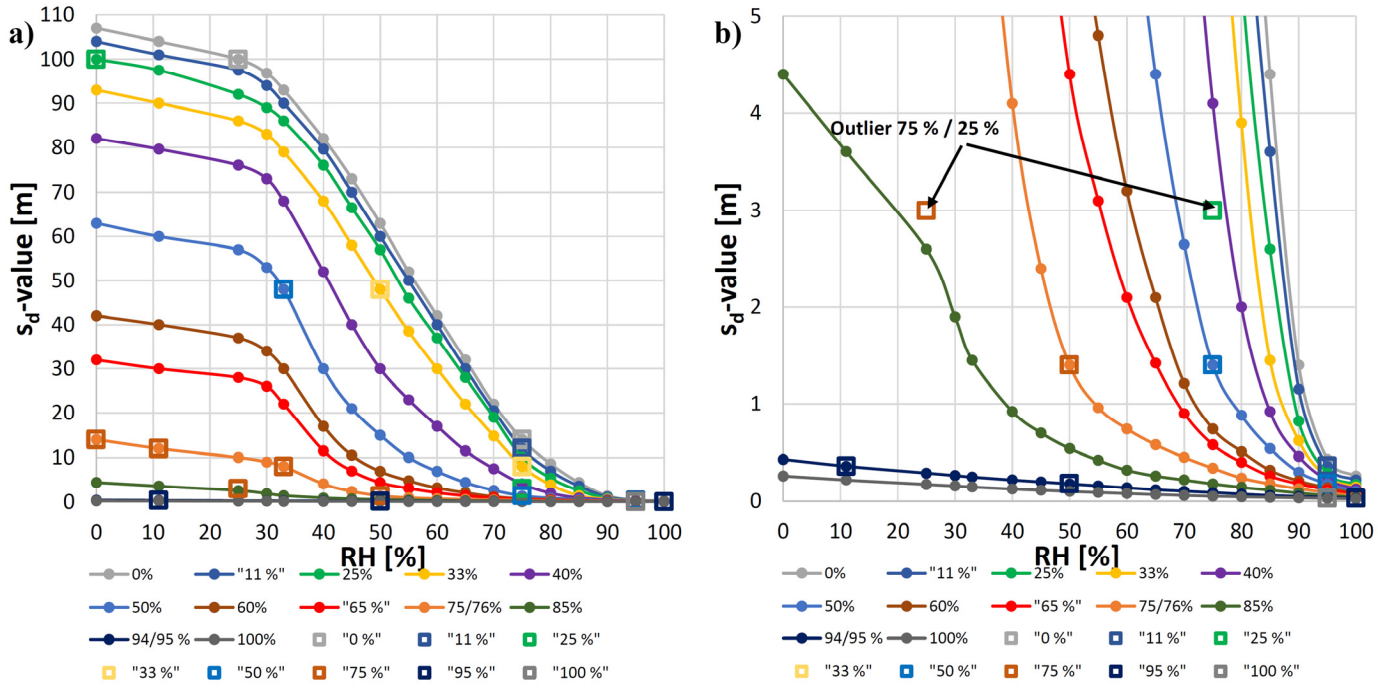

Figure A1. SVB s_d-value curves each plotted with a constant RH level on one side with varying RH on the other side; (**a**) full range on *y*-axis and (**b**) reduced range on *y*-axis. Values from Table A4 marked with dots. Measured values from technical approval document marked with squares.

Appendix C Model Algorithm Validation

Presentation of benchmark results is provided to support confidence in the hygrothermal model that is applied in the current article. The Hamstad benchmark 4 [70] has been chosen since this implements severe climate exposure, including moisture condensation, alternating rapid wetting and drying, in addition to moisture redistribution between two materials [44]. The benchmark is designed as a 1D benchmark, i.e., the heat and moisture transport are 1D directional. However, the benchmark has been run in COMSOL in 3D to verify that the model can handle 2D and 3D functionality. Still, it does not validate 3D directional heat and moisture transport per se. Full description of the benchmark can be found in [44,70] and will not be repeated.

Selected results of the benchmark validation are provided in Figure A2. The selection considers what are of particular interest for the current study; that is, validating handling of moisture front from severe rain absorption (see Figure A2e) and moisture redistribution (see Figure A2f,g).

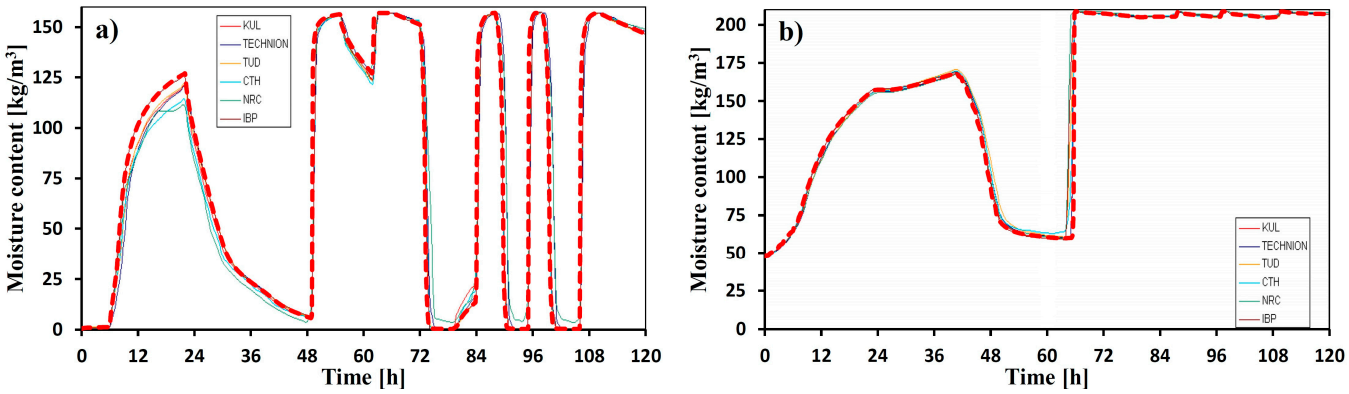

Figure A2. *Cont.*

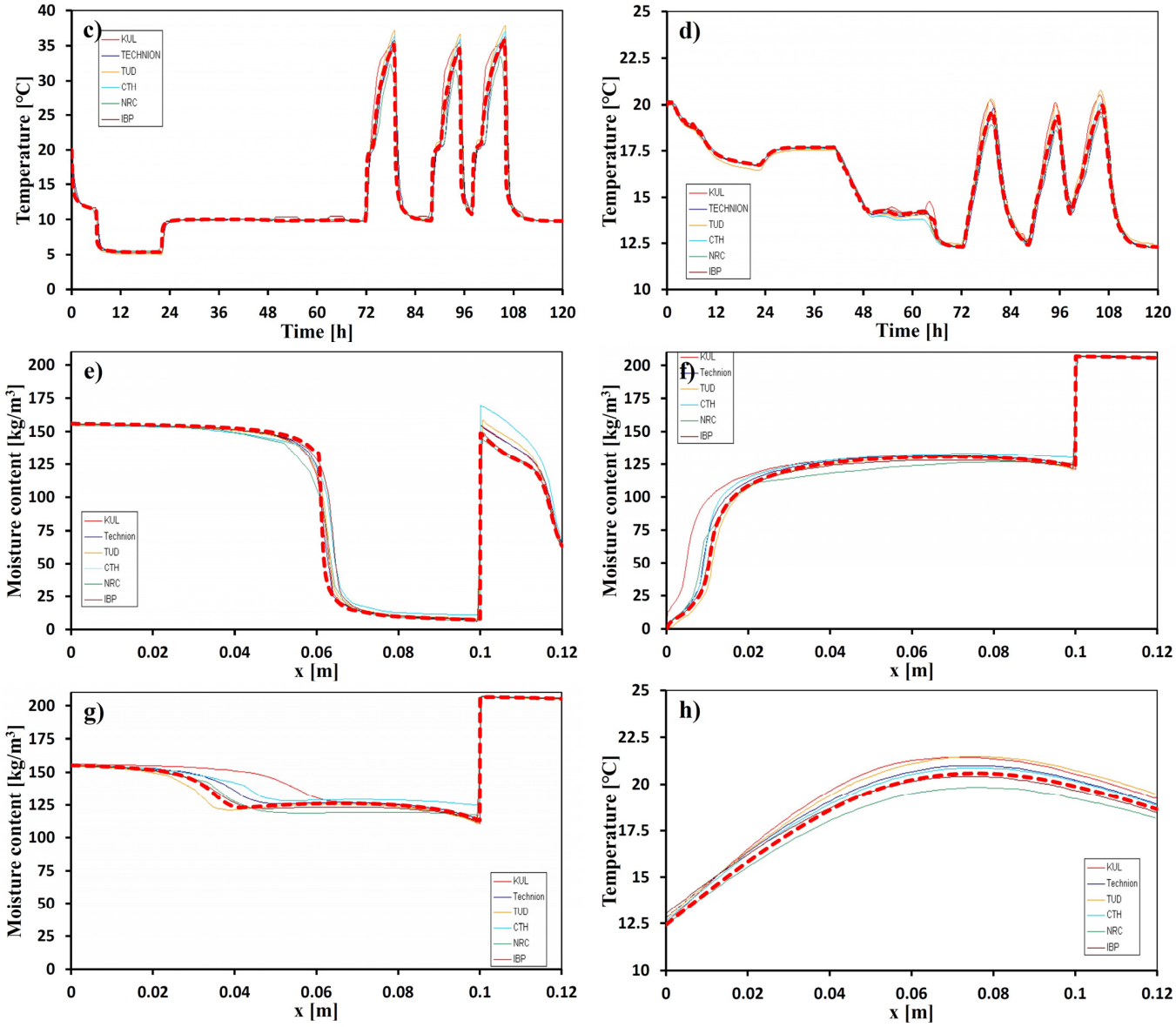

Figure A2. Model validation against Hamstad benchmark 4. Results, dashed red lines, are superimposed graphs from [70]. Moisture content (**a**) exterior surface, (**b**) interior surface, temperature (**c**) exterior surface, (**d**) interior surface, moisture profile at (**e**) 54 h, (**f**) 78 h, (**g**) 96 h, temperature profile at (**h**) 96 h.

References

1. Odgaard, T.; Bjarløv, S.P.; Rode, C. Interior insulation—Characterisation of the historic, solid masonry building segment and analysis of the heat saving potential by 1d, 2d, and 3d simulation. *Energy Build.* **2018**, *162*, 1–11. [CrossRef]
2. Harrestrup, M.; Svendsen, S. Full-scale test of an old heritage multi-storey building undergoing energy retrofitting with focus on internal insulation and moisture. *Build. Environ.* **2015**, *85*, 123–133. [CrossRef]
3. Harrestrup, M.; Svendsen, S. Internal insulation applied in heritage multi-storey buildings with wooden beams embedded in solid masonry brick façades. *Build. Environ.* **2016**, *99*, 59–72. [CrossRef]
4. Zhou, X.; Carmeliet, J.; Derome, D. Influence of envelope properties on interior insulation solutions for masonry walls. *Build. Environ.* **2018**, *135*, 246–256. [CrossRef]
5. Vereecken, E.; Roels, S. Wooden beam ends in combination with interior insulation: An experimental study on the impact of convective moisture transport. *Build. Environ.* **2019**, *148*, 524–534. [CrossRef]
6. Jensen, N.F.; Bjarløv, S.P.; Rode, C.; Møller, E.B. Hygrothermal assessment of four insulation systems for interior retrofitting of solid masonry walls through calibrated numerical simulations. *Build. Environ.* **2020**, *180*, 107031. [CrossRef]

7. Martel, T.; Rirsch, E.; Simmonds, A.; Walker, C. The monitoring of wall moisture in a property retrofitted with Internal Wall Insulation. *Case Stud. Constr. Mater.* **2021**, *14*, e00520. [CrossRef]
8. Zhou, X.; Derome, D.; Carmeliet, J. Analysis of moisture risk in internally insulated masonry walls. *Build. Environ.* **2022**, *212*, 108734. [CrossRef]
9. Johansson, P.; Wahlgren, P. Deterioration in brick buildings: Hygrothermal performance and measures to save them. In Proceedings of the 12th Nordic Symposium on Building Physics (NSB 2020), Tallinn, Estonia, 6–9 September 2020.
10. Huerto-Cardenas, H.E.; Leonforte, F.; Aste, N.; Del Pero, C.; Evola, G.; Costanzo, V.; Lucchi, E. Validation of dynamic hygrothermal simulation models for historical buildings: State of the art, research challenges and recommendations. *Build. Environ.* **2020**, *180*, 107081. [CrossRef]
11. Martín-Garín, A.; Millán-García, J.A.; Terés-Zubiaga, J.; Oregi, X.; Rodríguez-Vidal, I.; Baïri, A. Improving Energy Performance of Historic Buildings through Hygrothermal Assessment of the Envelope. *Buildings* **2021**, *11*, 410. [CrossRef]
12. Blocken, B.; Derome, D.; Carmeliet, J. Rainwater runoff from building facades: A review. *Build. Environ.* **2013**, *60*, 339–361. [CrossRef]
13. Calle, K.; Coupillie, C.; Janssens, A.; Van Den Bossche, N. Implementation of rainwater infiltration measurements in hygrothermal modelling of non-insulated brick cavity walls. *J. Build. Phys.* **2019**, *43*, 477–502. [CrossRef]
14. Kubilay, A.; Zhou, X.; Derome, D.; Carmeliet, J. Moisture modeling and durability assessment of building envelopes—Recent advantages. In *Building Performance Simulation for Design and Operation*, 2nd ed.; Jan, L.M.H., Roberto, L., Eds.; Routledge: London, UK, 2019; pp. 270–314.
15. Ramirez, R.; Ghiassi, B.; Pineda, P.; Lourenço, P.B. Experimental characterization of moisture transport in brick masonry with natural hydraulic lime mortar. *Build. Environ.* **2021**, *205*, 108256. [CrossRef]
16. Scheffler, G. *Validation of Hygrothermal Material Modelling under Consideration of the Hysteresis of Moisture Storage*; Dresden University of Technology: Dresden, Germany, 2008.
17. Knarud, J.I.; Kvande, T.; Geving, S. Modelling hydraulic conductivity for porous building materials based on a prediction of capillary conductivity at capillary saturation. *Int. J. Heat Mass Transf.* **2022**, *186*, 122457. [CrossRef]
18. Scheffler, G.A.; Plagge, R. A whole range hygric material model: Modelling liquid and vapour transport properties in porous media. *Int. J. Heat Mass Transf.* **2010**, *53*, 286–296. [CrossRef]
19. Van Belleghem, M.; Steeman, M.; Janssen, H.; Janssens, A.; De Paepe, M. Validation of a coupled heat, vapour and liquid moisture transport model for porous materials implemented in CFD. *Build. Environ.* **2014**, *81*, 340–353. [CrossRef]
20. Derluyn, H.; Janssen, H.; Carmeliet, J. Influence of the nature of interfaces on the capillary transport in layered materials. *Constr. Build. Mater.* **2011**, *25*, 3685–3693. [CrossRef]
21. Vereecken, E.; Roels, S. Hygric performance of a massive masonry wall: How do the mortar joints influence the moisture flux? *Constr. Build. Mater.* **2013**, *41*, 697–707. [CrossRef]
22. Brocken, H.J.P. *Moisture Transport in Brick Masonry: The Grey Area between Bricks*; Technische Universiteit Eindhoven: Eindhoven, The Netherlands, 1998.
23. Zhou, X.; Desmarais, G.; Vontobel, P.; Carmeliet, J.; Derome, D. Masonry brick–cement mortar interface resistance to water transport determined with neutron radiography and numerical modeling. *J. Build. Phys.* **2020**, *44*, 251–271. [CrossRef]
24. Kahangi Shahreza, S.; Niklewski, J.; Molnár, M. Novel water penetration criterion for clay brick masonry claddings. *Constr. Build. Mater.* **2022**, *353*, 129109. [CrossRef]
25. Groot, C.J.W.P.; Gunneweg, J.T.M. The influence of materials characteristics and workmanship on rain penetration in historic fired clay brick masonry. *Heron* **2010**, *55*, 141–153.
26. Hens, H.S.L.C. The vapor diffusion resistance and air permeance of masonry and roofing systems. *Build. Environ.* **2006**, *41*, 745–755. [CrossRef]
27. Vereecken, E.; Van De Walle, W.; Roels, S. A novel and flexible test setup to measure the vapour diffusion resistance of building materials and wall components. In Proceedings of the 4th Central European Symposium on Building Physics (CESBP 2019), Prague, Czech Republic, 2–5 September 2019.
28. Gutland, M.; Bucking, S.; Santana Quintero, M. A methodology for hygrothermal modelling of imperfect masonry interfaces. *J. Build. Phys.* **2021**, *44*, 485–509. [CrossRef]
29. Johansson, P.; Geving, S.; Hagentoft, C.-E.; Jelle, B.P.; Rognvik, E.; Kalagasidis, A.S.; Time, B. Interior insulation retrofit of a historical brick wall using vacuum insulation panels: Hygrothermal numerical simulations and laboratory investigations. *Build. Environ.* **2014**, *79*, 31–45. [CrossRef]
30. Knarud, J.I.; Geving, S.; Kvande, T. Moisture performance of interior insulated brick wall segments subjected to wetting and drying—A laboratory investigation. *Build. Environ.* **2021**, *188*, 107488. [CrossRef]
31. Zhao, J.; Plagge, R. Characterization of hygrothermal properties of sandstones—Impact of anisotropy on their thermal and moisture behaviors. *Energy Build.* **2015**, *107*, 479–494. [CrossRef]
32. Feng, C.; Janssen, H. Hygric properties of porous building materials (VII): Full-range benchmark characterizations of three materials. *Build. Environ.* **2021**, *195*, 107727. [CrossRef]
33. Hansen, T.K.; Bjarløv, S.P.; Peuhkuri, R.H.; Harrestrup, M. Long term in situ measurements of hygrothermal conditions at critical points in four cases of internally insulated historic solid masonry walls. *Energy Build.* **2018**, *172*, 235–248. [CrossRef]

34. Andreotti, M.; Bottino-Leone, D.; Calzolari, M.; Davoli, P.; Dias Pereira, L.; Lucchi, E.; Troi, A. Applied Research of the Hygrothermal Behaviour of an Internally Insulated Historic Wall without Vapour Barrier: In Situ Measurements and Dynamic Simulations. *Energies* **2020**, *13*, 3362. [CrossRef]
35. Defraeye, T.; Blocken, B.; Carmeliet, J. Influence of uncertainty in heat–moisture transport properties on convective drying of porous materials by numerical modelling. *Chem. Eng. Res. Des.* **2013**, *91*, 36–42. [CrossRef]
36. Vereecken, E.; Van Gelder, L.; Janssen, H.; Roels, S. Interior insulation for wall retrofitting—A probabilistic analysis of energy savings and hygrothermal risks. *Energy Build.* **2015**, *89*, 231–244. [CrossRef]
37. De Mets, T.; Tilmans, A.; Loncour, X. Hygrothermal assessment of internal insulation systems of brick walls through numerical simulation and full-scale laboratory testing. *Energy Procedia* **2017**, *132*, 753–758. [CrossRef]
38. COMSOL Inc. *COMSOL Multiphysics*; COMSOL Inc.: Stockholm, Sweden, 2021.
39. Knarud, J.I.; Geving, S. Implementation and Benchmarking of a 3D Hygrothermal Model in the COMSOL Multiphysics Software. *Energy Procedia* **2015**, *78*, 3440–3445. [CrossRef]
40. Knarud, J.I.; Geving, S. Comparative study of hygrothermal simulations of a masonry wall. *Energy Procedia* **2017**, *132*, 771–776. [CrossRef]
41. Künzel, H.M. *Simultaneous Heat and Moisture Transport in Building Components*; Fraunhofer IRB-Verlag: Stuttgart, Germany, 1995.
42. Tariku, F.; Kumaran, K.; Fazio, P. Transient model for coupled heat, air and moisture transfer through multilayered porous media. *Int. J. Heat Mass Transf.* **2010**, *53*, 3035–3044. [CrossRef]
43. Tariku, F. *Whole Building Heat and Moisture Analysis*; Concordia University: Montreal, QU, Canada, 2008.
44. Hagentoft, C.-E.; Kalagasidis, A.S.; Adl-Zarrabi, B.; Roels, S.; Carmeliet, J.; Hens, H.; Grunewald, J.; Funk, M.; Becker, R.; Shamir, D. Assessment method of numerical prediction models for combined heat, air and moisture transfer in building components: Benchmarks for one-dimensional cases. *J. Therm. Envel. Build. Sci.* **2004**, *27*, 327–352. [CrossRef]
45. Tsilingiris, P.T. Thermophysical and transport properties of humid air at temperature range between 0 and 100 °C. *Energy Convers. Manag.* **2008**, *49*, 1098–1110. [CrossRef]
46. *Fraunhofer WUFI 2D 4.2*; Fraunhofer IBP: Stuttgar, Germany, 2019.
47. Ruisinger, U.; Kautsch, P. Comparison of hygrothermal 2D- and 3D-simulation results with measurements from a test house. *E3S Web Conf.* **2020**, *172*, 08004. [CrossRef]
48. Zhou, X.; Carmeliet, J.; Derome, D. Assessment of moisture risk of wooden beam embedded in internally insulated masonry walls with 2D and 3D models. *Build. Environ.* **2021**, *193*, 107460. [CrossRef]
49. Janssen, H.; Blocken, B.; Carmeliet, J. Conservative modelling of the moisture and heat transfer in building components under atmospheric excitation. *Int. J. Heat Mass Transf.* **2007**, *50*, 1128–1140. [CrossRef]
50. Janssen, H. Comment on Cabrera et al. A User-Friendly Tool to Characterize the Moisture Transfer in Porous Building Materials: FLoW1D. *Appl. Sci.* **2020**, *10*, 5090, *Appl. Sci.* **2022**, *12*, 1123.
51. Piaia, J.C.Z.; Cheriaf, M.; Rocha, J.C.; Mustelier, N.L. Measurements of water penetration and leakage in masonry wall: Experimental results and numerical simulation. *Build. Environ.* **2013**, *61*, 18–26. [CrossRef]
52. *NS-EN 15026*; Hygrothermal Performance of Building Components and Building Elements. Assessment of Moisture Transfer by Numerical Simulation. Norwegian Standards: Oslo, Norway, 2007.
53. Zhou, X.; Derome, D.; Carmeliet, J. Robust moisture reference year methodology for hygrothermal simulations. *Build. Environ.* **2016**, *110*, 23–35. [CrossRef]
54. Johansson, P.; Lång, L.; Capener, C.-M. How well do mould models predict mould growth in buildings, considering the end-user perspective? *J. Build. Eng.* **2021**, *40*, 102301. [CrossRef]
55. Kalamees, T. *Hygrothermal Criteria for Design and Simulation of Buildings*; Tallinn University of Technology: Tallinn, Estonia, 2006.
56. Hens, H.S. Modeling the heat, air, and moisture response of building envelopes: What material properties are needed, how trustful are the predictions? *J. ASTM Int.* **2007**, *4*, 1–11. [CrossRef]
57. Marincioni, V.; Marra, G.; Altamirano-Medina, H. Development of predictive models for the probabilistic moisture risk assessment of internal wall insulation. *Build. Environ.* **2018**, *137*, 257–267. [CrossRef]
58. Janssen, H.; Freudenberg, P.; Tijskens, A.; Hou, T. *Basic Probabilistic Analysis of Hygrothermal Performance of Interior Insulation*; KU Leuven: Leuven, Belgium, 2019; p. 108.
59. *ISO 13823*; General Principles on the Design of Structures for Durability. ISO: Geneva, Switzerland, 2008.
60. Lacasse, M.A.; Morelli, M. A Systematic Method of Assessing the Durability of Wood-Frame Wall Assemblies: Towards the Limit-States Design Approach. In Proceedings of the Thermal Performance of the Exterior Envelopes of Whole Buildings XIII International Conference, Clearwater, FL, USA, 4–8 December 2016; pp. 235–245.
61. Lacasse, M.A.; Van Den Bossche, N.; Van Linden, S.; Moore, T.V. A brief compendium of water entry results derived from laboratory tests of various types of wall assemblies. In Proceedings of the 4th Central European Symposium on Building Physics (CESBP 2019), Prague, Czech Republic, 2–5 September 2019.
62. Nath, S.; Dewsbury, M.; Künzel, H.; Watson, P. Mould Growth Risks for a Clay Masonry Veneer External Wall System in a Temperate Climate. *Atmosphere* **2022**, *13*, 1755. [CrossRef]
63. Lacasse, M.A.; Ge, H.; Hegel, M.; Jutras, R.; Laouadi, A.; Sturgeon, G.; Wells, J. *Guideline on Design for Durability of Building Envelopes*; National Research Council (NRC) of Canada: Ottawa, ON, Canada, 2018.

64. Carmeliet, J.; Roels, S. Determination of the Moisture Capacity of Porous Building Materials. *J. Therm. Envel. Build. Sci.* **2002**, *25*, 209–237. [CrossRef]
65. Schirmer, R. *Die Diffusionszahl von Wasserdampf-Luft-Gemischen und Die Verdampfungsgeschwindigkeit*; Springer: Berlin/Heidelberg, Germany, 1938; pp. 170–177.
66. Grunewald, J.; Häupl, P.; Bomberg, M. Towards an Engineering Model of Material Characteristics for Input to Ham Transport Simulations—Part 1: An Approach. *J. Therm. Envel. Build. Sci.* **2003**, *26*, 343–366. [CrossRef]
67. Ghanbarian, B.; Daigle, H. Thermal conductivity in porous media: Percolation-based effective-medium approximation. *Water Resour. Res.* **2016**, *52*, 295–314. [CrossRef]
68. *EN 1745*; Masonry and Masonry Products—Methods for Determining Thermal Properties. CEN: Brussels, Belgium, 2012.
69. Yoshinaga, M. Performance of smart vapor retarders under hot and humid summer conditions. *Build. Environ.* **2022**, *218*, 109163. [CrossRef]
70. Hagentoft, C.-E. HAMSTAD, Final report: Methodology of HAM-modeling. In *Report R-02*; Chalmers University of Technology: Gothenburg, Sweden, 2002.